

1
2
3
4 **The relationship between latent heating, vertical velocity, and precipitation**
5 **processes: The impact of aerosols on precipitation in organized deep convective**
6 **systems**
7

8
9
10 Wei-Kuo Tao¹ and Xiaowen Li^{1,2}

11
12
13
14 *¹Mesoscale Atmospheric Processes Laboratory*
15 *NASA/Goddard Space Flight Center*
16 *Greenbelt, MD 20771, USA*
17

18
19 *²Goddard Earth Sciences Technology and Research*
20 *Morgan State University*
21 *Baltimore, MD, 21250, USA*
22

23
24 *Submitted to J. Geophys. Res.*

25
26 November 20, 2014

27 Revised September 23, 2015 and January 22, 2016

28
29
30
31 Corresponding author address: Dr. W.-K. Tao, Code 612,
32 Mesoscale Atmospheric Processes Laboratory, NASA/GSFC, Greenbelt, MD 20771
33 Email: Wei-Kuo.Tao-1@nasa.gov
34

35
36 Keywords: aerosol, CCN, precipitation, cold pool, latent heat, convection
37
38
39
40
41

42 **Key Points**

43
44 Increasing aerosol number concentrations could either enhance or reduce surface
45 precipitation. Enhanced near surface cold pool strength is important in precipitation
46 enhancement. Other processes include modifications of latent heat release and ice
47 microphysics by aerosols.

48
49
50 **Abstract**

51
52 A high-resolution, two-dimensional cloud-resolving model with spectral-bin
53 microphysics is used to study the impact of aerosols on precipitation processes in both a
54 tropical oceanic and a midlatitude continental squall line with regard to three processes:
55 latent heating (LH), cold pool dynamics and ice microphysics. Evaporative cooling in the
56 lower troposphere is found to enhance rainfall in low cloud condensation nuclei (CCN)
57 concentration scenarios in the developing stages of a midlatitude convective precipitation
58 system. In contrast, the tropical case produced more rainfall under high CCN
59 concentrations. Both cold pools and low-level convergence are stronger for those
60 configurations having enhanced rainfall. Nevertheless, latent heat release is stronger
61 (especially after initial precipitation) in the scenarios having more rainfall in both the
62 tropical and midlatitude environment. Sensitivity tests are performed to examine the
63 impact of ice and evaporative cooling on the relationship between aerosols, LH and
64 precipitation processes. The results show that evaporative cooling is important for cold
65 pool strength and rain enhancement in both cases. However, ice microphysics play a
66 larger role in the midlatitude case compared to the tropical. Detailed analysis of the

67 vertical velocity governing equation shows that temperature buoyancy can enhance
68 updrafts/downdrafts in the middle/lower troposphere in the convective core region;
69 however, the vertical pressure gradient force (PGF) is the same order and acts in the
70 opposite direction. Water loading is small but on the same order as the net PGF-
71 temperature buoyancy forcing. The balance among these terms determines the intensity
72 of convection.

73

74 **1. Introduction**

75

76 Aerosols are a critical factor in the atmospheric hydrological cycle and radiation budget.
77 As a major reason for clouds to form and a significant attenuator of solar radiation,
78 aerosols affect climate in several ways. Current research suggests that aerosol effects on
79 clouds could further extend to precipitation, both through the formation of cloud particles
80 and by exerting persistent radiative forcing on the climate system. However, the various
81 mechanisms behind these effects, in particular the ones connected to precipitation, are not
82 yet well understood [see reviews by *Levin and Cotton, 2008, Khain, 2009, and Tao et al.,*
83 *2012*].

84

85 Compared to typical global circulation and climate models, cloud-resolving models
86 (CRMs) use more sophisticated and relatively realistic representations of cloud
87 microphysical processes, and they can reasonably well resolve the structure and life
88 cycles of clouds and cloud systems (with sizes ranging from about 2-1000 km). CRMs
89 also allow for direct interaction among clouds, outgoing longwave (cooling) and
90 incoming solar (heating) radiation, as well as ocean and land surface processes [see
91 reviews by *Tao, 2003, 2007; Randall et al., 2003; and Tao and Moncrieff, 2009*]. There
92 are several major advantages in using CRMs to study the interactive processes between
93 clouds, precipitation and aerosols. For example, the use of a sophisticated microphysics
94 scheme (liquid and ice) and a fine horizontal resolution can provide relatively realistic
95 cloud optical properties, which are crucial for determining radiation budgets. With a high
96 spatial resolution, each atmospheric grid is considered either completely cloudy
97 (overcast) or clear; no partial cloudiness is assumed as with GCMs. In addition, the life

98 cycle of clouds, precipitation and aerosols can be simulated by CRMs. CRMs can also
99 have better cloud dynamic processes in terms of aerosol transport [see reviews by
100 *Thompson et al.*, 1997; *Ekman et al.*, 2004, 2006; and *Yin et al.*, 2005].

101

102 Recently, many different studies have used CRMs to examine the role of aerosols on
103 mixed-phase convective clouds (c.f., Table 1). These modeling studies have many
104 differences in terms of model configuration (two- vs three-dimensional, single case study
105 vs ensemble simulations), domain size, grid spacing (150 – 3000 m), microphysics (i.e.,
106 two-moment bulk, simple or sophisticated spectral-bin), turbulence (1st or 1.5 order
107 turbulent kinetic energy), radiation, lateral boundary conditions (i.e., closed, cyclic or
108 radiative open), cases (isolated convection vs organized systems) and model integration
109 time (e.g., from 2.5 to 48 up to 100s of hours in order to reach convective-radiative
110 equilibrium). A simple metric, the percent change in time-integrated precipitation ($dP =$
111 $100 * (P_{high} - P_{low}) / P_{low}$) as a result of a set increase in the number concentration of
112 CCN ($dN_0 = N_{high} - N_{low}$), has been used to examine the impact of aerosol concentration
113 on surface rainfall. $P_{high} - P_{low}$ is the difference in surface rainfall between the high and
114 low CCN concentrations, and $N_{high} - N_{low}$ is the number concentration difference between
115 the high and low CCN. Among these modeling studies, the most striking difference is
116 that cumulative precipitation can either increase or decrease in response to higher
117 concentrations of CCN. *Phillips et al.* [2002], *Khain et al.* [2004, 2005], *Khain and*
118 *Pokrovsky* [2004], *Teller and Levin* [2006], *Cheng et al.* [2010], *Fan et al.* [2013],
119 *Saleeby et al.* [2010], *Storer et al.* [2010], *Seigel et al.* [2013], and *Grant and van den*
120 *Heever* [2015] changed the number concentrations of CCN gradually and found robust

121 decreases in cumulative precipitation for higher concentrations of CCN. This is
122 completely opposite from the results from Wang [2005], Khain et al. [2005], Lee et al.
123 [2009], Fan et al. [2007b], Lebo and Morrison [2014], and Igel et al. [2013]. Variations
124 in the microphysics scheme, vertical wind shear, atmospheric static stability and relative
125 humidity (dry vs. moist) could lead to different aerosol impacts on precipitation [Storer et
126 al., 2010; Fan et al., 2012a,b; Storer and van den Heever, 2013; Kalina et al., 2014;
127 Grant and van den Heever, 2015]. Also, the different stages of a convective system's life
128 cycle may also respond differently to changes in aerosols in terms of precipitation [Tao et
129 al., 2007; van den Heever and Cotton, 2007]. Note that these modeling studies are for
130 different convective systems that developed in different environments, and the results are
131 based on different models and microphysical schemes

132

133 Different physical processes have been proposed to explain aerosol impacts on deep
134 convective precipitation. These processes include latent heating (LH), cold-pool
135 dynamics and ice microphysics. However, these hypotheses were based on different
136 models and different cases. *In this paper, three different hypotheses are examined using*
137 *the same model with the same microphysics scheme and same cases.* The relationships
138 between LH, convective updrafts and downdrafts and precipitation processes with
139 different aerosol concentrations, and the different physical processes responsible for the
140 aerosol impact on precipitation are also examined. CRM simulations based on two deep
141 convective precipitation systems from vastly different environments, one tropical oceanic
142 and one midlatitude continental, and that have differing surface rainfall responses to
143 changes in aerosols, will be used for this study.

144

145 The physical processes hypothesized to invigorate convection are reviewed in section 2.
146 Section 3 describes the model and cases used in this study. The results including
147 sensitivity tests on evaporative cooling, and the summary, are presented in sections 4 and
148 5, respectively.

149

150 **2. Physical Processes Responsible for the CCN Effect on Precipitation**

151

152 In general, three mechanisms have been proposed to explain the enhancement of
153 precipitation due to changes (increased or decreased) in the aerosol concentration and are
154 described in the following subsections.

155

156 *2.1 Latent Heating Effect*

157

158 The first mechanism is the creation of stronger updrafts/downdrafts resulting from
159 enhanced latent heat release for high-CCN scenarios. This effect can be termed *the latent*
160 *heat – dynamic effect*, which includes LH from both condensational growth and the
161 freezing of water drops. Wang [2005], Rosenfeld *et al.*, [2008] and Li *et al.* [2013]
162 indicated that precipitation increases in tropical deep convection due to higher CCN
163 concentrations through this latent heat effect. Khain *et al.* [2005] also found that for
164 cases where there were enhanced precipitation with higher CCN concentrations, clouds
165 were associated with stronger updrafts/downdrafts as well as stronger convergence in the
166 boundary layer, which increases the chance to trigger secondary clouds and prolong the
167 lifetime of convective systems. Van den Heever and Cotton [2007], Lee *et al.* [2008] and

168 *Storer et al.* [2010] also demonstrated the influence of aerosols on secondary storm
169 development and its effect on increasing precipitation.

170

171 2.2 *Cold Pool Effect*

172

173 The second mechanism is based on the potential for stronger evaporative cooling due to
174 more but smaller cloud droplets under high CCN concentration conditions. Stronger
175 evaporative cooling can enhance the strength of the near surface cold pool. When the
176 enhanced cold pool interacts with low-level wind shear, convergence can become
177 stronger, producing more vigorous convection that ultimately leads to enhanced surface
178 precipitation [i.e., *Khain et al.*, 2005, *Tao et al.*, 2007]. This positive feedback
179 mechanism is termed the *cold pool effect*. Note that stronger evaporative cooling occurs
180 in the *developing stages of convective cloud systems*. *Lee et al.* [2009] also demonstrated
181 that stronger evaporative cooling occurred under higher aerosol concentrations and
182 consequently lead to enhanced surface precipitation. *Lebo and Morrison* [2014] showed
183 that changes in aerosol loading could alter raindrop size and number concentration, which
184 can affect cold pool strength via changes in evaporation. The balance between the cold
185 pool and low-level wind shear–induced vorticity [*Rotunno et al.*, 1988] can therefore be
186 changed by an aerosol perturbation. However, there are other studies (both modeling and
187 observational) in the literature that find that under higher CCN concentrations there are
188 fewer but larger raindrops, reduced evaporation rates and therefore warmer cold pools
189 [e.g., *Altaratz et al.*, 2007, *Storer et al.*, 2010; *May et al.*, 2011; *Saleeby et al.*, 2010,
190 *Khain et al.*, 2011, *Morrison*, 2012, *Loftus and Cotton*, 2014, *Grant and Van den Heever*,
191 2015].

192

193 2.3 *Cold Microphysics Effect*

194

195 The third mechanism is the CCN effect on ice-phase microphysics. For example, *Wang*
196 [2005] and *Rosenfeld et al.* [2008] suggested that with higher CCN concentrations, there
197 is a greater increase in total water content consisting of numerous small liquid particles.
198 This leads to less efficient collision-coalescence and hence less raindrop formation,
199 which allows for more droplets to be carried above the freezing level and become
200 supercooled where they can then enhance riming. This can then enhance latent heat
201 release via freezing. Among the major microphysical conversion processes, riming is
202 found to be most sensitive to aerosol concentration [*Cheng et al.*, 2010]. As a result, rain
203 production is mainly from ice phase microphysics. *Cheng et al.* [2010] further showed
204 that increasing the CCN concentration leads to more cloud droplets and cloud ice. *Storer*
205 *and van den Heever* [2013] also showed that the collision and coalescence processes and
206 the production of rain from ice are sensitive to aerosol concentrations. The impact of
207 changes in cloud droplets and cloud ice on the resulting surface precipitation is termed
208 the cold microphysics effect.

209

210 The three physical mechanisms can affect each other, making it difficult to isolate each
211 mechanism independently. For example, stronger evaporative cooling (the cold pool
212 effect) can be due to more evaporation associated with stronger convective downdrafts
213 (the latent heating effect). The cold microphysics effect can affect both the latent heating
214 and the cold pool effect and vice-versa. More numerous cloud droplets (due to more
215 CCN) can also lead to more ice nucleation and thus a higher number of snow and graupel

216 particles which, when melted, form more but smaller raindrops that cause stronger
217 evaporative cooling below the cloud base. Convection may be strengthened due to either
218 the latent heating effect or the cold pool effect with the induced stronger updrafts then
219 leading to higher super-saturation and thus enhanced ice deposition and nucleation.

220

221 **3. Numerical model and cases**

222

223 *3.1 Model*

224

225 The model used in this study is the same as in *Tao et al.* [2007]. It is the two-
226 dimensional (2D) version of the Goddard Cumulus Ensemble (GCE) model. The
227 equations that govern the cloud-scale motion are anelastic by filtering out sound waves.
228 The subgrid-scale turbulence used in the model is based on *Klemp and Wilhelmson*
229 [1978]. The effect of condensation on the generation of subgrid-scale kinetic energy is
230 also incorporated into the model [*Soong and Ogura*, 1980]. The model includes
231 interactive solar [*Chou et al.*, 1998] and thermal infrared [*Chou and Suarez*, 1994]
232 radiation parameterization schemes.

233

234 The spectral-bin microphysics developed by *Khain et al.* [2005] has been implemented
235 into the GCE model [*Tao et al.*, 2007 and *Li et al.*, 2009]. Its ice-phase collection
236 coefficients have been modified based on comparisons with radar observations [*Li et al.*,
237 2010]. The collisional growth formulation is based on solving stochastic kinetic
238 equations for the size distributions of water droplets (cloud droplets and raindrops), and
239 six types of ice particles: pristine ice crystals (columnar and plate-like), snow (dendrites
240 and aggregates), graupel, and frozen drops/hail. In the scheme, hail is high density and

241 originates from the direct freezing of water drops and grows via the collection of super-
 242 cooled water while graupel is moderate density and forms when snow aggregates collect
 243 super-cooled water droplets. Each hydrometeor type is described by a size distribution
 244 using 33 categories (mass bins). Size spectra of atmospheric aerosols are also described
 245 using 33 bins. The initial aerosol size distribution is represented by the sum of 3
 246 lognormal distributions [Jaenicke, 1993]:

$$n(\log D) = \sum_{i=1}^3 \frac{N_i}{(2\pi)^{\frac{1}{2}} \log \sigma_i} \exp \left(-\frac{(\log D - \log \bar{D}_i)^2}{2 \log^2 \sigma_i} \right)$$

247 where D is the particle diameter, N is the number concentration, and σ is the standard
 248 deviation of the log-normal distributions. The subscript i represents three different size
 249 modes in atmospheric aerosols: the Aitken mode, the accumulation mode and the coarse
 250 mode. This size distribution (activation) is different from that used in *Tao et al.* [2007].
 251 The marine background spectrum ($N_i=133, 66.6, \text{ and } 3.1 \text{ cm}^{-3}$; $D_i = 0.008, 0.266 \text{ and } 0.58$
 252 μm , and $\log \sigma_i = 0.657, 0.210 \text{ and } 0.396$) is used for the TOGA COARE control case, and
 253 the remote continental spectrum ($N_i=3200, 2900, \text{ and } 0.3 \text{ cm}^{-3}$; $D_i = 0.02, 0.116 \text{ and } 1.8$
 254 μm , and $\log \sigma_i = 0.161, 0.217 \text{ and } 0.380$) is used for the PRESTORM control case. In the
 255 high CCN scenarios, the background number concentrations are simply increased by 10
 256 fold. Aerosol concentration is held constant with height for particles with radius smaller
 257 than $2\mu\text{m}$. The large aerosol concentration is constant from the surface to 1 km, and then
 258 decreases exponentially with an e-folding factor of 2 km.

259
 260 The aerosol spectra were taken from *Jaenicke* [1993] and are compilations of ground
 261 measurements at various locations. These spectra are based on data from different
 262 observations and are normalized consistently. Since aerosol observations are not

263 available for either PRESTORM or TOGA COARE cases, these observation-based
264 aerosol concentrations were used to represent aerosol concentrations in different
265 environmental conditions (oceanic vs. continental). The high values in the remote
266 continental spectrum are mainly in the Aitken mode and accumulation mode. There are
267 two pieces of evidence that suggest that these values are not saturating the aerosol effect.
268 First, only the coarse mode and the tail (large sizes) of the accumulation mode become
269 activated in the PRESTORM case. The actual cloud droplet concentrations are
270 comparable to the previous study [*Tao et al.*, 2007] where an idealized $CCN=C*S^k$
271 spectrum was used. Second, similar small aerosol effects were presented in *Tao et al.*
272 [2007] for the same PRESTORM case with $C=600\text{ cm}^{-3}$ for the low-CNN scenario and
273 6000 cm^{-3} for the high-CNN scenario. The vertical aerosol distributions of aerosols are
274 based on field observation results [i.e., *Fridlind et al.*, 2012]. Aerosols enter and exit via
275 the open lateral boundaries. The lower boundary is held constant. Aerosol wet
276 deposition is included in the simulations, but dry deposition is ignored. The environment
277 becomes cleaner after precipitation passes through.

278

279 All scalar variables (potential temperature, mixing ratio of water vapor, turbulence
280 coefficients, and all hydrometeor classes) use forward time differencing and a positive
281 definite advection scheme with a non-oscillatory option [*Smolarkiewicz and Grabowski*,
282 1990]. The dynamic variables, u and w , use a fourth-order accurate advection scheme
283 and leapfrog time integration. Details of the GCE model description and improvements
284 can be found in *Tao and Simpson* [1993] and *Tao et al.* [2014].

285

286 Radiative open lateral boundary conditions are used [*Klemp and Wilhelmson, 1978*]. A
287 large horizontal domain is used in this study to simulate the large convective system and
288 minimize the reflection of convectively-generated gravity waves at the lateral boundaries
289 [see *Fovell and Ogura, 1988*]. The top boundary condition is free slip (i.e., the vertical
290 velocity is assumed to be zero as are the vertical gradients of horizontal wind velocity
291 and other scalar variables). In addition, a Rayleigh relaxation (or damping) layer is
292 applied above 15 km to damp convectively-generated gravity waves near the top of the
293 model domain, which is above 20 km. There are 1024 horizontal grid points with a
294 resolution of 1 km in the center 720 points and laterally-stretched grids on either side.
295 Use of the stretched horizontal grid makes the model less sensitive to the choice of
296 gravity wave speed associated with the open lateral boundary conditions [*Fovell and*
297 *Ogura, 1988*]. For the present study, a stretched vertical coordinate with 33 levels is
298 used. The model has finer resolution (80 and 40 meters for the PRESTORM and TOGA
299 COARE cases, respectively) in the boundary layer and coarser resolution (about 1000
300 meters) at upper levels. The model time step is 5 s. Convection is initiated by imposing
301 a cold air mass at the beginning of the simulation, imitating the cold pool dynamics that
302 generate new convection at the leading edge of the respective squall lines.

303

304 3.2 Cases

305

306 Two cases from vastly different environments, a tropical oceanic squall system observed
307 during TOGA COARE (the Tropical Ocean and Global Atmosphere Coupled Ocean-
308 Atmosphere Response Experiment, which occurred over the Pacific Ocean warm pool
309 from November 1992 to February 1993), and a midlatitude continental squall system

310 observed during PRESTORM (the Preliminary Regional Experiment for STORM-
311 Central, which occurred in Kansas and Oklahoma during May-June 1985), are used to
312 identify the physical processes that are responsible for enhancing the precipitation
313 processes associated with deep convective systems as a result of changing CCN
314 concentrations.

315

316 The 22 February 1993 TOGA COARE squall line has been well studied [*Jorgensen et al.*,
317 1997; *Redelsperger et al.*, 2000; *Trier et al.*, 1996, 1997; *Wang et al.*, 1996, 2003]. The
318 sounding used to initialize the model is from *LeMone et al.* [1994]. Surface fluxes are
319 included in the model for this case using the TOGA COARE flux algorithm [*Fairall et*
320 *al.*, 1996; *Wang et al.*, 1996]. The 10-11 June 1985 PRESTORM case has also been well
321 studied [e.g., *Johnson and Hamilton*, 1988; *Rutledge et al.*, 1988; *Tao et al.*, 1995, 1996;
322 *Yang and Houze*, 1995; *Lang et al.*, 2003]. The PRESTORM environment is fairly
323 unstable and relatively dry. The model is initialized with a single sounding taken at 2330
324 UTC from Pratt, KS, which was taken ahead of the squall line. Radiation is included but
325 not surface fluxes. The freezing level is approximately 4.5 km for the TOGA COARE
326 case and 3 km for the PRESTORM case. Both the TOGA COARE and PRESTORM
327 cases are well-organized, long-lived mesoscale convective systems. These two cases
328 were also simulated by *Tao et al.* [2007] and found to have different responses to changes
329 in CCN concentration.

330

331 The two cloud systems presented in this study formed into organized, linear structures
332 (i.e., squall lines). A 2D simulation, therefore, can provide a reasonable approximation
333 of their line-normal structure. Since the real atmosphere is 3D, further 3D cloud-

334 resolving simulations are still needed to address aerosol-precipitation interactions. In
335 addition, a finer resolution and large domain are required to solidify interactive aerosol-
336 cloud-precipitation processes further.

337

338 3.3 *Numerical Experiments*

339

340 A total of ten numerical experiments are conducted; Table 2 shows the numerical
341 experiments (names), their descriptions and domain mean rainfall amount. The first two (P-
342 low and P-high) experiments are for the PRESTORM case using low and high CCN
343 concentrations, respectively. The third and fourth (T-low and T-high) are for the TOGA
344 COARE case using low and high CCN concentrations, respectively. The next four
345 experiments (P-low-warm, P-high-warm, T-low-warm, and T-high-warm) are the same as the
346 first four experiments except that they use warm rain physics only. The P-low-evap and T-
347 high-evap cases are used to examine the impact of evaporation processes on aerosol-
348 precipitation interaction. More discussion on the numerical experiments is presented in the
349 following section.

350

351 **4. Results**

352

353 Figure 1 shows time sequences of the model-estimated domain mean surface rainfall rate
354 for the TOGA COARE and PRESTORM cases. Note that there are some minor
355 differences between these and previous results published in *Tao et al.* [2007]. These
356 differences are due to the use of a different CCN activation. Nevertheless, the main
357 results are the same between this and the *Tao et al.* [2007] study. For example, rain

358 suppression in the high CCN concentration (i.e., polluted environment) runs is evident in
359 both studies for both cases but only during the first hour of the simulations, while rain
360 reaches the ground early in both studies for low CCN situations for both cases. Also,
361 during the mature stage of the simulations, the effect of increasing the CCN concentration
362 ranges from rain suppression in the PRESTORM case to rain enhancement in the TOGA
363 COARE case (see Table 2 for the detailed amounts for this study). These results still
364 indicate that model simulations of the whole life cycle of convective system are needed in
365 order to assess the impact of aerosols on precipitation processes. Please see *Tao et al.*
366 [2007, 2012] for more discussion.

367

368 4.1 *Latent heating and evaporative cooling effects*

369

370 Total LH consists of condensation, deposition, and freezing. Time series of total LH for
371 the high- and low-CCN scenarios are shown in Fig. 2 for the TOGA COARE case. The
372 model results clearly show that the total LH in the T-high scenario is much larger than
373 that for the T-low during the 12 h model integration. In addition, the mean total LH
374 profiles show that heating reaches higher in altitude, indicating taller cloud tops and
375 stronger convection for the T-high simulation. Figures 2(c) and (d) also indicate that the
376 low-level evaporative cooling is quite different between the T-low and T-high scenarios.
377 The high CCN scenario shows stronger, deeper evaporative cooling profiles than the low
378 (also see Fig. S1 in the supplement). Stronger evaporative cooling can enhance the near
379 surface cold-pool strength. When the cold pool interacts with the low-level wind shear,
380 the convergence could become stronger, producing stronger convection in the T-high
381 case (see Fig. S2 in the supplement). This can lead to more vigorous precipitation and

382 therefore enhanced surface precipitation (i.e., a positive feedback).

383

384 Rain suppression in the PRESTORM high CCN concentration (i.e., polluted
385 environment) run is evident for the P-high scenario (Fig. 1b). The total LH in the P-high
386 scenario is slightly weaker than in the P-low at upper levels (\sim above 7 km) during the
387 12-h model integrations (Figs. 3a and b). The evaporative cooling is also slightly weaker
388 at low altitude (surface to 3 km) for the high-CCN run (Figs. 3c and d). These results are
389 completely opposite to the TOGA COARE case wherein stronger evaporative cooling
390 and LH occur in the high-CCN run. In addition, the total LH and evaporative cooling are
391 much stronger in the PRESTORM case than those in the TOGA COARE case. This
392 result is due to the high convective available potential energy (CAPE) and drier
393 environmental in the PRESTORM case (see Table 3 in *Tao et al.* 2007).

394

395 More rain reaches the surface after an hour and a half of model integration in the T-high
396 simulation as compared to the T-low simulation (Fig. 1a). During this period, more
397 evaporative cooling in the T-high simulation is already evident from the model results
398 (Fig. 2d). Figures 4(a) and (b) show the vertical profiles of the time and domain mean
399 LH and evaporative cooling during the early stage of the simulated TOGA COARE high
400 and low CCN scenarios. During the first hour of model integration, evaporative cooling
401 is stronger (2-3 K/day), and LH is also slightly stronger (less than 0.5 K/day) for the T-
402 high scenario. Evaporative cooling is still stronger and occurs in a narrow area near the
403 leading edge of the system for the T-high run for the first two hours of model integration
404 (see Fig. S1 in the supplement). The strongest evaporative cooling for the T-low run is
405 not at the leading edge of the system. The strongest LH occurs in a narrow region and at

406 the leading edge of the system for both the T-high and T-low scenarios (see Fig. S1 in the
407 supplement), but LH is much stronger for the T-high scenario than the T-low after 1.5 h
408 model integration. Peak LH is between 2 and 5 km and indicates development of low-
409 level cloud (warm-rain) during the first two hours of model integration (Fig. 2). Note
410 that the strongest LH occurs between 2 and 3 hours of model integration for the T-high
411 scenario (Fig. 2a).

412

413 The total LH profiles, especially above 5 km, are quite similar for the low and high-CCN
414 scenarios during the first 1 to 2.5 hours of model integration for PRESTORM case (Fig.
415 4c). But, the total LH is stronger (1-2 K/day) between 2 and 4 km for the P-low scenario.
416 The evaporative cooling is also stronger at lower levels in the P-low run for the
417 PRESTORM case (Fig. 4d). This could be related to the early onset of rainfall in that run
418 and because rain evaporation dominates the lower levels for this case. Note that the
419 results show that there are less small rain (< 2 mm) droplets for the P-high scenario than
420 the P-low. In addition, the strongest evaporative cooling is located in a very narrow
421 region at the leading edge after 3.5 hours of model integration in the P-low run in contrast
422 to the P-high (see Fig. S3 in the supplement). The results also show that strong LH
423 occurs within a narrow region and at the leading edge of each system for both the P-high
424 and P-low runs as with the TOGA COARE runs (see Fig. S3 in the supplement)

425

426 The role of total LH and evaporative cooling with regard to enhancing surface rainfall is
427 examined during the developing/early stages of the TOGA COARE and PRESTORM
428 cases. For TOGA COARE, LH is slightly larger for the high-CCN scenario than the low;

429 however, low-level evaporative cooling is stronger for the high-CCN scenario. The low-
430 level evaporative cooling and its interaction with the low-level convergence zone could
431 be the key physical process that enables more surface rainfall to be generated for the
432 TOGA COARE squall line under high aerosol loading. For the PRESTORM case, P-low
433 does have more small raindrops. It also has more low-level evaporative cooling compared
434 to P-high. Also, with the dry environment in the PRESTORM case, evaporation rates
435 will be high in both the clean and polluted scenarios, and hence the impact of aerosols
436 may be reduced. In contrast, the moist environment limits the evaporation rates in the
437 TOGA COARE case such that aerosols may be required to make droplets sufficiently
438 small in order to achieve reasonable evaporation rates [Tao *et al.*, 2007].

439

440 Figure 5 shows Hovmoller diagrams of low-level convergence and low-level equivalent
441 potential temperature perturbations for the P-low and P-high simulations. The low-level
442 equivalent potential temperature perturbations (averaged vertically from the lowest model
443 level to $z=3$ km) can be used as an indicator of the cold pool strength. Only the first 4
444 hours of data are plotted here in order to emphasize details of the cold pool structures
445 because the differences in surface rainfall (Fig. 1b) and evaporative cooling (Figs. 3c and
446 d) already emerged within this time. Figures 5e and 5f also show the vertical structure of
447 the equivalent potential temperature perturbations and convective updrafts (contour lines
448 at 1, 5 and 10 m/s). Both cases simulate a narrow, linear convective system. The low-
449 level convergence and cold pool are both stronger in the P-low scenario than in the P-
450 high scenario. These features are clearly shown after 1.5 hours of model
451 integration. Evaporative cooling at the lowest levels is also stronger in the P-low case

452 after 1.5 hours (Figs. 3c and 3d) as is the surface rainfall (Fig. 1b). The highest surface
453 rainfall rates are located in the low-level convergence zone. The vertical cold pool
454 structure is only slightly stronger in the P-low scenario than the P-high scenario. The
455 convective updrafts are located near and above the cold pool. There are also remnants of
456 convective cells above the cold pool and over a broad area that extends 100 km from the
457 leading edge of the system. This feature has been observed [i.e., *Rutledge et al.*, 1988
458 and *Johnson and Hamilton*, 1988] and simulated by many CRMs [i.e., *Dudhia et al.*,
459 1987; *Rotunno et al.*, 1988; *Lafore and Moncrieff*, 1989 and many others]. Note that the
460 maximum convective updrafts are quite similar between the P-high and P-low scenarios
461 [shown in Fig. 3 in *Tao et al.*, 2007]. The small differences in maximum updrafts are due
462 to the PRESTORM environment being fairly unstable with a CAPE of 2300 J/kg.

463

464 There are similarities and differences between the PRESTORM and TOGA COARE
465 cases in terms of low-level convergence, cold pools, and the vertical structures of the
466 simulated systems (Fig. 6). Both the PRESTORM and TOGA COARE cases have
467 narrow low-level convergence zones, cold pools at the leading edge of the system and
468 convective updrafts located above the cold pools. However, the cold pools and
469 convective updrafts are much weaker in the TOGA COARE case due to a weaker CAPE
470 (1776 J/kg) as compared with the PRESTORM case. Also, surface rainfall was enhanced
471 in the high CCN simulation, T-high, which was not the case for PRESTORM. Low-level
472 convergence is stronger in the T-high simulation than in the T-low (Fig. 6 a and b). It is
473 much stronger than in the T-low after 1.5 hours of model integration. The low-level cold
474 pool is also stronger in the T-high run than in the T-low between 0.5 and 1.5 hours of

475 model integration. This is consistent with the evaporative cooling shown in Fig. 2. There
476 is more rainfall (i.e., enhancement) in the T-high scenario than in the T-low after 1.5
477 hours of model integration (Fig. 1a). Figure 6 also shows that the cold pool is “warmer”
478 at the leading edge of the stronger convergence zone in the T-low scenario. The cold
479 pool is “colder” at the leading edge of or close to the stronger convergence zone in the T-
480 high scenario, especially after initial stage of model simulations. This feature is also
481 shown in the vertical structures (Figs. 6e and f) and is the reason for the more upright
482 vertical velocity structure shown in Fig. 6f. Therefore, the enhanced cold pool (driven by
483 evaporative cooling) interacting with convergence can allow for new (or secondary)
484 clouds to be deeper. This could also enhance rainfall in the T-high scenario (compared to
485 the T-low) in the TOGA COARE precipitation system.

486

487 4.2 *Warm Rain Only*

488

489 The third hypothesis regarding the invigoration of convective precipitation systems in
490 high CCN environments is the cold microphysics effect. Sensitivity experiments are
491 performed by turning off the ice processes to examine the impact of ice microphysics on
492 aerosol-precipitation interactions (similar tests were conducted in *Tao et al.*, [2007]). In
493 these sensitivity tests, the following microphysical processes are included: (1)
494 condensation/evaporation of liquid drops, (2) drop/drop collision/coalescence, (3)
495 turbulence effects on liquid drop collisions, (4) collisional breakup, and (5) sedimentation
496 of liquid. These warm-rain only tests still allow condensation to occur above the freezing
497 level in place of deposition. In addition, the warm rain scenario does not allow riming
498 and freezing processes, which result in more cold rain and melting. Therefore, the

499 differences between the pairs of control runs (low CCN vs. high CCN) and the warm-rain
500 only runs can be used to assess and examine the role of ice microphysics in producing the
501 sensitivities between the low-CCN and high-CCN environments.

502

503 Figure 7 shows time sequences of model-estimated domain mean surface rainfall rate
504 without ice processes (warm rain only). For the PRESTORM case, the mean surface
505 rainfall under both low CCN and high CCN conditions is quite similar. This suggests
506 that the ice processes are crucial in suppressing surface precipitation and increasing the
507 portion of light rain in a high-CCN environment. For TOGA COARE, rain suppression
508 due to a high CCN concentration is again only evident during the first hour or so of the
509 simulation. For the entire period, increasing CCN still enhances rainfall, the same as
510 with the full ice run. These results suggest that the main mechanisms for CCN enhancing
511 surface rainfall exist in warm rain microphysics. However, ice-phase microphysics can
512 further enhance the surface rainfall amount in the T-high scenario as compared with the
513 T-high-warm scenario, because the majority of surface rainfall in this case comes from
514 warm rain.

515

516 The total LH and evaporative cooling (Figs. 2 and 8) for the TOGA COARE case for the
517 low-CCN scenario are quite similar between the control and warm rain only simulations
518 and indicate that ice processes appear to play only a secondary role in terms of their
519 aerosol impact in this scenario. The total LH between the control and warm rain only
520 simulations for the high-CCN scenario is likewise similar for the first 1.5 hours of model
521 integration. Thus, during the development and early mature stages of the high CCN
522 simulations, ice processes again appear to have little impact on the aerosol effect as LH

523 and evaporative cooling are nearly identical to the full physics control run (Figs. 2b and
524 d). However, after 2 hours of simulation, the total LH in the high CCN full physics
525 control run is larger and deeper, especially above the freezing level where there are more
526 episodes of deep, LH penetrations, than in the warm rain only simulation. Likewise,
527 Figs. 2d and 8d indicate that the low-level evaporative cooling becomes quite different
528 with the warm rain run exhibiting much stronger and somewhat deeper (as evaporation
529 replaces sublimation above the freezing level in the warm rain run) low-level
530 evaporation, which in turn enhances the near surface cold-pool. The difference between
531 the low- and high-CCN simulations (Figs. 8c and d) is greater than that between the
532 control pair (Figs. 2c and d). As in the control run, evaporative cooling, which affects
533 cell regeneration in convective systems, is still determined mainly by warm rain
534 processes for the TOGA COARE case.

535

536 For the PRESTORM warm rain experiments, the differences in total LH and evaporative
537 cooling are not significant between the P-high-warm and P-low-warm cases (Fig. 9). The
538 differences are quite small during the first 3 hours (early stage) of the model simulations.
539 This could be the reason for the similar surface rainfall between the high and low CCN
540 situations. Note that there is a jump in latent heat release around 4 and 5 hour,
541 respectively, for the low and high CCN cases. Consequently, there is enhanced
542 evaporative cooling and surface rainfall. The difference in LH and evaporative cooling is
543 quite small because the PRESTORM environment is both fairly unstable with a
544 convective available potential energy (CAPE) of 2300 J/kg and relatively dry and
545 therefore already conducive for evaporation. In addition, these results also suggest that

546 ice microphysics play an important role in the aerosol impact for the PRESTORM case.

547

548 These warm-rain only sensitivity tests still allow condensation to occur above the
549 freezing level in place of deposition. These tests examine the water phase microphysics;
550 their associated latent heating and evaporative cooling are responsible for the greater
551 sensitivity shown in the TOGA COARE case in contrast to the PRESTORM case. *Khain*
552 *and Sednev* [1996] applied spectral bin microphysics to a precipitation event that
553 occurred in the eastern Mediterranean coastal zone. Their results also showed that ice
554 processes did not have a significant effect on the location of precipitation events, the
555 vertical velocity or rainfall accumulation. However, their results did show that ice
556 processes can delay precipitation formation and alter the spatial distribution of
557 precipitation.

558

559 4.3 *The effect of latent heating on vertical velocity*

560

561 With the LH effect, updrafts/downdrafts could be enhanced as a result of enhanced latent
562 heat release. The relationship between thermodynamic buoyancy (or latent heat release)
563 and convective updrafts and downdrafts is analyzed to identify whether or not LH is the
564 main physical process enhancing surface rainfall due to aerosol-precipitation interactions.

565 The vertical velocity equation is shown as follows:

$$\frac{\partial w}{\partial t} = -\frac{\partial}{\partial x}uw - \frac{1}{\bar{\rho}}\frac{\partial}{\partial z}\bar{\rho}ww - C_p\bar{\theta}\frac{\partial\pi'}{\partial z} + g\left(\frac{\theta'}{\bar{\theta}} + 0.61q'_v - q_l\right) + D_w$$

566

567 where, u , and w are the horizontal and vertical velocity, the variables θ and q_v are
568 potential temperature and water vapor, $\bar{\rho}$ is the air density, $\bar{\pi} = (p/p_{00})^{R/c_p}$ is non-

569 dimensional pressure (where p and p_{oo} are dimensional and reference pressures,
570 respectively, with p_{oo} taken as 1000 hPa), c_p is the specific heat of dry air at constant
571 pressure, q_l is the liquid and ice water loading, and D_w is diffusion (turbulence term). The
572 prime means the deviation from the horizontal mean (represented by the bar over a
573 variable). Please see Soong and Ogura [1973, 1980] and Tao and Soong [1986] for
574 details on this equation. The turbulence term is very small and the advection term also
575 small in the middle and upper troposphere compared to the pressure gradient force and
576 buoyancy term. In the lower troposphere, the advection term is about 1/3 of the pressure
577 gradient force. It is positive (i.e., it acts to increase vertical velocity) beneath 1.5 – 2 km
578 and negative (i.e., it acts to decrease vertical velocity) above that.

579

580 Figure 10 shows the vertical pressure gradient force ($\text{PGF} = -C_p \bar{\theta} \frac{\partial \pi'}{\partial z}$), buoyancy effect
581 due to temperature buoyancy forcing or latent heat release ($g \frac{\theta'}{\bar{\theta}}$), water vapor buoyancy
582 force ($0.61 g q'_v$), and water loading effect ($-g q_l$) for the PRESTORM case. Both
583 buoyancy due to water vapor and the loading effect are quite small compared to PGF and
584 LHR. LHR is positive (negative) in the middle (low) troposphere where the convective
585 updrafts (downdrafts) are located. This implies that latent heat release (heating by
586 condensation and/or deposition) will enhance updrafts in the middle troposphere while
587 negative LH (i.e., cooling by evaporation) will enhance downdrafts in the low
588 troposphere. The buoyancy due to water vapor change is positive (negative) in the
589 middle (low) troposphere (Fig. 10c). It has the same effect on convective drafts as the
590 LH effect except with one order smaller magnitude. It also has a smaller effect than the
591 loading effect.

592

593 Figure 11(a) shows the domain mean vertical profiles of PGF and the LH effect for the
594 low-CCN and high-CCN scenarios. Both PGF and LH are slightly larger in the low-CCN
595 scenario than in the high-CCN scenario. Their net effect on updrafts and downdrafts is
596 about the same (Fig. 11(b)). Their net effect is also about the same magnitude as the
597 loading effect. This suggests that the loading effect is quite important but in a negative
598 way with regard to convective updraft enhancement. The relative roles of the PGF, LH
599 effect, water vapor buoyancy force and water loading effect on the vertical velocity are
600 the same for the TOGA COARE case.

601

602 The relationship between thermodynamic buoyancy (latent heat release), vertical pressure
603 gradient force, and drag from water loading associated with convective updrafts and
604 downdrafts has been previously studied [*Soong and Ogura, 1973; Schlesinger, 1980;*
605 *Knupp and Cotton, 1985; Tao et al., 1995 and Storer and van den Heever, 2013*]. For
606 example, *Soong and Ogura [1973]* showed the importance of the PGF on cloud
607 development. Their results also indicated that PGF is the same order of magnitude as the
608 thermal buoyancy force in the core regions of clouds. PGF acted in the opposite direction
609 of the net force due to the excess heat, moisture, and weight of liquid water (there were
610 no ice processes in their model). *The current modeling results are consistent with Soong*
611 *and Ogura [1973] except that the importance of the water loading effect has been*
612 *identified.*

613

614 *Tao et al. [1995]* also showed that PGF and buoyancy oppose each other and are larger
615 than the water loading. They suggested that the water-loading effect plays an important

616 role for initiating downdrafts. Their study was focused on cloud downdrafts and was
617 based on *trajectory analyses*. Recently, *Storer and van den Heever* [2013] indicated that
618 the drag associated with condensate loading is an important factor in determining the
619 *average updraft strength* for tropical deep convective clouds.

620

621 4.4 *Reduction of evaporative cooling*

622

623 Evaporative cooling from rain is one of the major microphysics processes that produce
624 cold pools in the lower troposphere. It is also one of the hypotheses associated with the
625 enhancement of precipitation and surface rainfall due to aerosols. Sensitivity tests in
626 terms of reduced evaporation are conducted. These tests aim to identify whether
627 evaporative cooling is the main physical process enhancing surface rainfall due to
628 aerosol-precipitation interactions. Note that in spectral-bin microphysics, water drops
629 and their interactions with one another span the whole size spectrum. There is no clear
630 distinction between cloud droplets and raindrops, and thus evaporative cooling comes
631 from the entire size spectrum (i.e., from small cloud droplets to large precipitating
632 raindrops). Reduced evaporation can impact surface rainfall in three ways. First, it could
633 allow more / larger raindrops to reach the surface. This could produce more surface
634 rainfall. Second, it could allow less cooling in the low troposphere and consequently
635 affect relative humidity (and reduce relative humidity due to a higher temperature), but it
636 could also allow for more evaporative cooling due to a lower relative humidity. This
637 could either favor or not favor the enhancement of precipitation processes and therefore
638 surface rainfall. Third, the cold pool strength could be weakened. This could affect
639 secondary convective generation and reduce the surface rainfall (the hypothesis discussed

640 in the 2nd section). Which factor dominates could depend on the large-scale (or
641 mesoscale) environment.

642

643 In the first sensitivity test, evaporation is completely removed from 1 to 3 hours of model
644 integration, from the surface to 3 km, for the PRESTORM P-low scenario. This is
645 because evaporative cooling is quite similar between the P-low and P-high simulations
646 during the first hour of model integration (see Fig. 3). Figure 12 shows time sequences of
647 the model-estimated domain mean surface rainfall rate for the three different scenarios
648 (P-low, P-high and P-low-evap, which is P-low without evaporation from 1 to 3 hours
649 from 0 to 3 km). The total rainfall amount is reduced from 58.4 mm for the (clean)
650 control simulation to 40.7 mm for the reduced evaporation simulation. In the P-low-evap
651 scenario, rainfall increased significantly after the first hour of model integration due to
652 the first impact (more/larger raindrops reach the surface). After 3 hours, when
653 evaporation is turned back on, rainfall is initially reduced due to the reverse of the first
654 impact (fewer/smaller raindrops reach the surface); however, rainfall continues at a
655 reduced rate until the cold pool is replenished (figure not shown) and eventually increases
656 back to a level similar to the clean scenario at around 7 hours.

657

658 For the TOGA COARE case, T-high is used to show the sensitivity to evaporation. P-
659 low and T-high have the most rainfall and evaporation for their respective cases and
660 therefore are likely to show the greatest response to changes in evaporation. For the T-
661 high case, the evaporation rate is reduced 100 % only for the first 1.5 hours of model
662 integration, from the surface to a height of 4 km. The results show that the total amount
663 of accumulated surface precipitation is reduced (from 33.0 mm to 26.6 mm) compared to

664 the T-high run (Fig. 13). The results also show that rainfall increased significantly for the
665 first one and half hours of model integration due to the first impact of reduced
666 evaporation (more rainfall reaches the surface) and are consistent with the PRESTORM
667 case. The rainfall amount was also only slightly reduced compared to the T-high
668 scenario but is still more than the T-low after 1.5 hour of model integration. Eventually,
669 the rainfall amount and temporal variation of the surface rainfall is quite similar between
670 the simulation without evaporation and the clean run after 6.5 hours of model integration
671 (Fig. 13). Different environmental conditions (moist vs. dry, differing stability or
672 convective available potential energy) could be the reason for this difference.
673 Evaporative cooling is quite efficient and could have more impact on convective systems
674 in a drier environment (i.e., the P-high scenario).

675

676 An additional run with evaporation reduced by 50% over the first 1.5 hours of model
677 integration was also conducted for the T-high scenario. Rainfall is almost identical
678 between these two runs even after the first 1.5 hours of model integration (plot not
679 shown). This is because the temporal domain-mean LH and evaporative cooling are quite
680 similar (Fig. 14). Both cases should have smaller-sized droplets due to high CCN
681 concentrations. By reducing evaporation, some of the smaller drops will remain, and
682 hence light rainfall will be possible. It should also reduce the relative humidity and
683 therefore allow more evaporative cooling to occur later on. This could explain why the
684 evaporative cooling does not change in these two cases. Consequently, the LH does not
685 change significantly either (Figs. 14b and c).

686

687 **5. Summary**

688

689 A 2D CRM with detailed spectral-bin microphysics is used to examine and identify the
690 dominant physical processes that determine precipitation enhancement as a result of high
691 CCN concentrations. Two cases are simulated using idealized initial aerosol
692 concentrations: a tropical, linear convective system during TOGA COARE and a
693 summertime, midlatitude squall line during PRESTORM. A pair of model simulations,
694 an experiment with low (clean) and an experiment with high CCN concentrations
695 (polluted environment), is conducted for each case. The latent heating and evaporative
696 cooling associated with three different potential processes (i.e., latent heating, cool-pool
697 and ice microphysics) that could determine the aerosol impact on deep convective
698 precipitation are examined. The relationship between vertical velocities, vertical pressure
699 gradient force, buoyancy (latent heat and water vapor) and the water loading effect are
700 also examined to identify the important processes for convective development.
701 Sensitivity tests are performed to examine the impact of ice and evaporative cooling on
702 the relationship between aerosols and precipitation processes. The major highlights are
703 as follows:

704

- 705 • For the scenarios in which rainfall is enhanced (i.e., T-high and P-low), low-level
706 cold pools and convergence are stronger than in their counterpart scenarios (i.e., T-
707 low and P-high). The low-level evaporative cooling is also stronger in the T-high and
708 P-low cases, especially in the early stages (i.e., the first 1-3 hours of model
709 integration) of the convective systems. The results also suggest that latent heating
710 and evaporative cooling (and cold pools) are the key processes associated with the
711 enhanced rainfall during the *mature stage* of these two deep convective, precipitating

712 cloud systems (i.e., Figs. 2 and 3). The importance of latent heating and evaporative
713 cooling over the *whole life cycle* of convective cloud systems was also addressed in
714 *Khain* [2009].

715 • For the TOGA COARE (tropical) case, the T-high-warm scenario still produces more
716 rainfall than the T-low-warm as with the original full physics simulations. This is
717 because the latent heating and evaporative cooling are quite similar between the ice
718 and warm rain only simulations. This result suggests that the ice processes do not
719 have a major impact on aerosol-precipitation interaction for this case. For the
720 PRESTORM (midlatitude) case, the P-high-warm and P-low-warm simulations
721 produce similar total rainfall amounts. In contrast, the P-high and P-low simulations
722 have much larger differences. This suggests that ice processes are crucial in
723 suppressing surface precipitation in the high CCN environment.

724 • For both the PRESTORM (P-low) and TOGA COARE (T-high) high rainfall
725 scenarios, the total rainfall amount is reduced in sensitivity tests in which evaporation
726 is restricted (see Table 2). However, rainfall increased significantly during the period
727 in which evaporation was eliminated because more rain could reach the surface. The
728 simulated cold pools are also much weaker compared to the run with full evaporation
729 in the PRESTORM case. The results also show that overall rainfall was still more
730 than in the high (low) CCN scenario for the PRESTORM (TOGA COARE) case.
731 This is because the cold pool was replenished and eventually become stronger.
732 Similar to other studies [e.g., *Khain et al.*, 2005; *Khain*, 2009], our results suggest
733 that evaporative cooling can affect the cold pool strength.

734 • For both the TOGA COARE and PRESTORM cases, the temperature buoyancy term
735 can enhance updrafts via heating due to condensation and deposition in the middle
736 troposphere and downdrafts via evaporative cooling in the lower troposphere in the
737 convective core region (see Fig. 10). However, PGF is the same order of magnitude
738 as the temperature buoyancy forcing and acts in the opposite direction. This suggests
739 that PGF is as important as the temperature buoyancy term in determining the cloud
740 velocity strength. The water loading and water vapor buoyancy terms are quite small
741 compared to PGF and temperature buoyancy forcing. *But, the water loading term is*
742 *the same order as the net difference between PGF and temperature buoyancy forcing.*
743 This suggests that the water-loading effect could be quite important for vertical
744 velocities associated with clouds. These results are consistent with previous
745 modeling results for isolated clouds [Soong and Ogura, 1973], from trajectory
746 analysis [Tao et al., 1995], and for multi-cloud systems [Storer and van den Heever,
747 2013].

748
749 Almost all previous CRM studies (including the present one) used idealized chemical
750 compositions and CCN concentrations in the simulations [e.g., van den Heever et al.,
751 2006]. Furthermore, the spatial distribution of CCN was assumed to be uniform, at
752 least horizontally. A non-homogeneous CCN distribution (from observations or from
753 large-scale modeling/analyses), consistent with non-homogeneous initial
754 meteorological conditions, is needed to assess aerosol-precipitation interactions [i.e.,
755 Shi et al., 2014]. A 2D simulation provides a good approximation to the observed
756 linear convective systems in this study; however, 3D CRM simulations are needed to
757 address aerosol-precipitation interactions more fully. Furthermore, CRM studies

758 need to compare model results with observed cloud features such as dynamical and
759 microphysical profiles, cloud extent, evolution of organization, radar reflectivity, and
760 rainfall. Combining observations and modeling can enable us to better understand the
761 response of clouds and precipitation to aerosols and their interactive feedbacks.

762

763 **Acknowledgments:**

764

765 This research was supported by the NASA Precipitation Measurement Missions (PMM),
766 the NASA Modeling, Analysis, and Prediction (MAP) Program, and the Office of
767 Science (BER), U.S. Department of Energy/Atmospheric System Research (DOE/ASR)
768 Interagency Agreement (No. DE-AI02-04ER63755). The authors are grateful to Drs.
769 Ramesh Kakar and David B. Considine at NASA headquarters for their support of this
770 research. Acknowledgment is also made to the NASA Goddard Space Flight Center and
771 NASA Ames Research Center computing facilities and to Dr. Tsengdar Lee at NASA HQ
772 for the computational resources used in this research. We would like to thank Drs. J. Fan
773 and S. van den Heever for updating Table 1 and Mr. Stephen Lang for proofing the
774 manuscript. We also thank three anonymous reviewers for their constructive comments
775 that improved this paper significantly. All simulation data are freely available upon
776 request to: xiaowen.li@nasa.gov.

777

778

779 **References:**

780 Altaratz, O., I. Koren, and T. Reisin, (2007), Aerosols' influence on the interplay
781 between condensation, evaporation and rain in warm cumulus cloud. *Atmos. Chem.*

782 *Phys.*, **7**, 12 687–12 714.

783 Cheng, C.-T., W.-C. Wang, and J.-P. Chen (2010), Simulation of the effects of increasing
784 cloud condensation nuclei on mixed-phase clouds and precipitation of a front system,
785 *Atmos. Res.*, **96**, 461-476, doi:10.1016/j.atmosres.2010.02.005.

786 Chou, M.-D., and M. J. Suarez (1994), An efficient thermal infrared radiation
787 parameterization for use in general circulation models. *NASA Tech. Memo. 104606*,
788 *85pp.*

789 Chou, M.-D., M. J. Suarez, C.-H. Ho, M.-H. Yan, and K.-T. Lee (1998),
790 Parameterizations for Cloud Overlapping and Shortwave Single-Scattering Properties
791 for Use in General Circulation and Cloud Ensemble Models, *J. Clim.*, **11**, 202-214.

792 Dudhia, J., M. M. W, and D. W. K. So (1987), The two-dimensional dynamics of West
793 African squall lines. *Quart. J. Roy. Meteor. Soc.*, **113**, 121-146.

794 Ekman, A., C. Wang, J. Storm, and R. Kreici (2006), Explicit simulation of aerosol
795 physics in a cloud-resolving model: Aerosol transport and processing in the free
796 troposphere; *J. Atmos. Sci.*, **63**, 682-696.

797 Ekman, A., C. Wang, J. Wilson, and J. Strom (2004), Explicit simulation of aerosol
798 physics in a cloud-resolving model: A sensitivity study based on an observed
799 convective cloud, *Atmos. Chem. Phys.*, **4**, 773-791.

800 Fairall, C. W., E. F. Bradley, D. P. Rogers, J. B. Edson, and G. S. Young (1996), Bulk
801 parameterization of air-sea fluxes for Tropical Ocean Global Atmosphere Coupled
802 Ocean-Atmosphere Response Experiment, *J. Geophys. Res.*, **101**, 915-929.

803 Fan, J, R. Zhang, G. Li, W.-K. Tao, and X. Li (2007), Simulation of cumulus clouds
804 using a spectral microphysics cloud-resolving model, *J. Geophys. Res.*, **112**, D04201,
805 doi:10.1029/2006JD007688.

806 Fan, J., T. Yuan, J. M. Comstock, S. Ghan, et al. (2009), Dominant role by vertical wind
807 shear in regulating aerosol effects on deep convective clouds, *J. Geophys. Res.*, **114**,
808 D22206, doi:10.1029/2009JD012352.

809 Fan J., L.Y.R. Leung, Z. Li, H. Morrison, H. Chen, Y. Zhou, Y. Qian, and Y.
810 Wang (2012a), Aerosol impacts on clouds and precipitation in Eastern China: Results
811 from bin and bulk microphysics, *J. Geophys. Res. D. (Atmospheres)*, **117**, D00K36,
812 doi:10.1029/2011JD016537.

813 Fan J., D. Rosenfeld, Y. Ding, L.Y.R. Leung, and Z. Li (2012b), Potential aerosol
814 indirect effects on atmospheric circulation and radiative forcing through deep
815 convection, *Geophys. Res. Lett.*, **39**, L09806, doi:10.1029/2012GL051851.

816 Fan J., L.Y.R. Leung, D. Rosenfeld, Q. Chen, Z. Li, J. Zhang, and H. Yan (2013),
817 Microphysical effects determine macrophysical response for aerosol impacts on deep
818 convective clouds, *Proc. National Acad. Sci.*, **110**(48), E4581-E4590,
819 doi:10.1073/pnas.1316830110.

820 Fovell, R. G. and Y. Ogura (1988), Numerical simulation of a midlatitude squall line in
821 two dimensions. *J. Atmos. Sci.*, **45**, 3846-3879.

822 Fridlind, A. M., A. S. Ackerman, J.-P. Chaboureau, J. Fan, W. W. Grabowski, A. A. Hill,
823 T. R. Jones, M. M. Khaiyer, G. Liu, P. Minnis, H. Morrison, L. Nguyen, S. Park, J. C.
824 Petch, J.-P. Pinty, C. Schumacher, B. J. Shipway, A. C. Varble, X. Wu, S. Xie, and

825 M. Zhang (2012), A comparison of TWP-ICE observational data with cloud-resolving
826 model results. *J. Geophys. Res.*, **117**, D05204, doi:10.1029/2011JD016595.

827 Grant, L.D. and S.C. van den Heever (2014), Aerosol-cloud-land surface interactions
828 within tropical sea breeze convection. *J. Geophys. Res.*, **119**, 8340-8361.

829 Grant, L.D., and S.C. van den Heever (2015), Cold pool and precipitation responses to
830 aerosol loading: modulation by dry layers. *J. Atmos. Sci.*, **72**, 1398-1408.

831 Igel, A. L., S. C. Van Den Heever, C. M. Naud, S. M. Saleeby, and D. J. Posselt (2013),
832 Sensitivity of warm-frontal processes to cloud-nucleating aerosol concentrations, *J.*
833 *Atmos. Sci.*, **70**, 1768-1783.

834 Jaenicke, R. (1993), Tropospheric aerosols. *Aerosol-Cloud-Climate Interactions*. Hobbs,
835 P. V. (ed.), Academic Press, 1-31.

836 Johnson, R. H., and P. J. Hamilton (1988), The relationship of surface pressure features
837 to the precipitation and airflow structure of an intense midlatitude squall line, *Mon.*
838 *Wea. Rev.*, **116**, 1444-1472.

839 Jorgensen, D. P., M. A. LeMone, and S. B. Trier (1997), Structure and evolution of the
840 22 February 1993 TOGA COARE squall line: Aircraft observations of precipitation,
841 circulation, and surface fluxes, *J. Atmos. Sci.*, **54**, 1961-1985.

842 Kalina, E. A., K. Friedrich, H. Morrison, and G. H. Bryan (2014), Aerosol effects on
843 idealized supercell thunderstorms in different environments. *J. Atmos. Sci.*, **71**, 164-
844 186.

845 Khain, A.P. and I. Sednev (1996), Simulation of precipitation formation in the Eastern
846 Mediterranean coastal zone using a spectral microphysics cloud ensemble model,
847 *Atmos. Res.*, **43**, 77-110.

848 Khain, A., A. Pokrovsky, M. Pinsky, A. Seigert, and V. Phillips (2004), Simulation of
849 effects of atmospheric aerosols on deep turbulent convective clouds using a spectral
850 microphysics mixed-phase cumulus cloud model. Part I: Model description and
851 possible applications. *J. Atmos. Sci.*, **61**, 2983-3001.

852 Khain, A., and A. Pokrovsky (2004), Simulation of effects of atmospheric aerosols on
853 deep turbulent convective clouds using a spectral microphysics mixed-phase cumulus
854 cloud model. Part II: Sensitivity study. *J. Atmos. Sci.*, **61**, 2963-2982.

855 Khain, A., D. Rosenfeld, and A. Pokrovsky (2005), Aerosol impact on the dynamics and
856 microphysics of deep convective clouds. *Q. J. R. Meteorol. Soc.*, **131**, 1-25.

857 Khain, A. P. (2009), Effects of aerosols on precipitation: a review. *Environ. Res. Lett.* **4**,
858 doi: 10.1088/1748-9326/4/1/015004.

859 Khain, A. P., D. Rosenfeld , A. Pokrovsky, U. Blahak , A. Ryzhkov (2011), The role of
860 CCN in precipitation and hail in a mid-latitude storm as seen in simulations using a
861 spectral (bin) microphysics model in a 2D dynamic frame [Atmospheric Research 99](#)
862 [\(2011\) 129–146](#).

863 Klemp, J. B., and R. B. Wilhelmson (1978), The simulation of three-dimensional
864 convective storm dynamics. *J. Atmos. Sci.*, **35**, 1070-1096.

865 Knupp, K. R., and W. R. Cotton (1985), Convective cloud downdraft structure: An
866 interpretive survey. *Rev. Geophys.*, **23**, 183-215.

867 Lafore, J.-P., and M. W. Moncrieff (1989), A numerical investigation of the organization
868 and interaction of the convective and stratiform regions of tropical squall lines. *J.*
869 *Atmos. Sci.*, **46**, 521-544.

870 Lang, S., W.-K. Tao, J. Simpson, and B. Ferrier (2003), Modeling of convective-
871 stratiform precipitation processes: Sensitivity to partitioning methods. *J. Appl.*
872 *Meteor.*, **42**, 505-527.

873 Lebo, Z. J. and H. Morrison (2014), Dynamical effects of aerosol perturbations on
874 simulated idealized squall lines, *Mon. Wea. Rev.*, **142**, 991-1009, doi:10.1175/MWR-
875 D-13-00156.1, 2014.

876 Lee, S. S., and G. Feingold (2010), Precipitating cloud-system response to aerosol
877 perturbations, *Geophys. Res. Lett.*, **37**, L23806, doi:10.1029/2010GL045596.

878 Lee, S. S., L. J. Donner, V. T. J. Phillips, and Y. Ming (2008), Examination of aerosol
879 effects on precipitation in deep convective clouds during the 1997 ARM summer
880 experiment, *Q. J. R. Meteorol. Soc.*, **134**(634), doi: 10.1002/qj.287.

881 Lee, S. S., L. J. Donner, and V.T. J. Phillips (2009), Impacts of aerosol chemical
882 composition on microphysics and precipitation in deep convection, *Atmos. Res.*, **94**,
883 doi.org/10.1016/j.atmosres.2009.05.015.

884 LeMone, M. A., D. P. Jorgensen, and B. F. Smull (1994), The impact of two convective
885 systems of sea surface stresses in COARE. *Preprints, Sixth Conf. On Mesoscale*
886 *Processes, Portland, OR, Amer. Meteor. Soc.*, 40-44.

887 Levin, Z., and W. R. Cotton (2009), Aerosol pollution impact on precipitation: A
888 scientific review, *Springer*, 386pp.

889 Li, X., W.-K. Tao, A. Khain, J. Simpson, and D. Johnson (2009), Sensitivity of a cloud-
890 resolving model to the bulk and explicit bin microphysical schemes. Part I.
891 Comparisons. *J. Atmos. Sci.*, **66**, 3-21.

892 Li, X., W.-K. Tao, T. Matsui, C. Liu, and H. Masunaga (2010), Improving a spectral bin
893 microphysical scheme using long-term TRMM satellite observations. *Quart. J. Roy.*
894 *Meteor. Soc.*, **136**, 382-399.

895 Li, X., W.-K. Tao, H. Masunaga, G. Gu, and X. Zeng (2013), Aerosol Effects on
896 Cumulus Congestus Population over the Tropical Pacific: A Cloud-Resolving
897 Modeling Study. *J. Meteor. Soc. Japan*, **91**(6), 817-833.

898 Loftus, A. M., and W.R. Cotton (2014), Examination of CCN impacts on hail in a
899 simulated supercell storm with triple-moment hail bulk microphysics, *Atmos. Res.*,
900 **147-148**, 183-204.

901 Lynn, B. H., A. Khain, J. Dudhia, D. Rosenfeld, A. Pokrovsky, and A. Seifert (2005),
902 Spectral (bin) microphysics coupled with a mesoscale model (MM5) part II:
903 Simulation of a CaPE rain event with a squall line, *Mon. Weather Rev.*, **133**, 59-71.

904 May, P. T., V. N. Bringi, and M. Thurai, (2011), Do we observe aerosol impacts on
905 DSDs in strongly forced tropical thunderstorms? *J. Atmos. Sci.*, **68**, 1902-1910.

906 Morrison, H., and W. W. Grabowski, (2011), Cloud-system resolving model simulations
907 of aerosol indirect effects on tropical deep convection and its thermodynamic
908 environment. *Atmos. Chem. Phys.*, **11**, 10503-10523, doi:10.5194/acp-11-10503-2011.

909 Morrison, H., (2012), On the robustness of aerosol effects on an idealized supercell storm
910 simulated with a cloud system-resolving model. *Atmos. Chem. Phys.*, **12**, 7689-7705,
911 doi:10.5194/acp-12-7689-2012.

912 Phillips, V. T. J., T. W. Choullarton, A. M. Blyth, and J. Latham (2002), The influence of
913 aerosol concentrations on the glaciation and precipitation of a cumulus cloud, *Q. J. R.*
914 *Meteorol. Soc.*, **128**(581), 951-971.

915 Randall, D., M. Khairoutdinov, A. Arakawa and W. Grabowski (2003), Breaking the
916 cloud parameterization deadlock, *Bull. Amer. Meteor. Soc.*, **84**, 1547-1564,
917 doi:10.1175/BAMS-84-11-1547.

918 Redelsperger, J.-L., and Co-authors (2000), A GCS model intercomparison for a
919 tropical squall line observed during TOGA-COARE. Part I: Cloud-resolving models.
920 *Quar. J. Roy. Meteor. Soc.*, **126**, 823-863.

921 Rosenfeld, D., U. Lohmann, G. B. Raga, C. D. O'Dowd, M. Kulmala, S. Fuzzi, A.
922 Reissell, and M. O. Andreae (2008), Flood or drought: How do aerosols affect
923 precipitation? *Science*, **321**, 1309-1313.

924 Rotunno, R., J. B. Klemp, and M. L. Weisman (1988), A theory for strong, long-lived
925 squall lines. *J. Atmos. Sci.*, **45**, 463-485.

926 Rutledge, S. A., R. A. Houze, Jr., and M. I. Biggerstaff (1988), The Oklahoma-Kansas
927 mesoscale convective system of 10-11 June 1985: Precipitation structure and single-
928 doppler radar analysis, *Mon. Wea. Rev.*, **116**, 1409-1430.

929 Saleeby, S. M., W. Berg, S. Van Den Heever, and T. L'ecuyer (2010), Impact of cloud-
930 nucleating aerosols in cloud-resolving model simulations of warm-rain precipitation
931 in the East China Sea. *J. Atmos. Sci.*, **67**, 3916-3930.

932 Schlesinger, R. E. (1980), A three-dimensional numerical model of an isolated
933 thunderstorm. Part II: Dynamics of updraft splitting and mesovortex couplet
934 evolution. *J. Atmos. Sci.*, **37**, 395-420.

935 Seigel, R.B., S.C. van den Heever, and S.M. Saleeby (2013), Mineral dust indirect effects
936 and cloud radiative feedbacks of a simulated idealized nocturnal squall line, *Atmos.*
937 *Chem. Phys.*, **13**, 4467-4485.

938 Shi, J. J., T. Matsui, W.-K. Tao, C. Peters-Lidard, M. Chin1, Q. Tan, and E. Kemp

939 (2014), Implementation of an Aerosol-Cloud Microphysics-Radiation Coupling into
940 the NASA Unified WRF: Simulation Results for the 6-7 August 2006 AMMA
941 Special Observing Period, *Quart. J. Roy. Meteor. Soc.*, **140**, 2158-2175.
942 doi: 10.1002/qj.2286

943 Smolarkiewicz, P. K., and W. W. Grabowski (1990), The multidimensional positive
944 advection transport algorithm: Nonoscillatory option. *J. Comput. Phys.*, **86**, 355-375.

945 Soong, S.-T., and Y. Ogura (1973), A comparison between axisymmetric and slab-
946 symmetric cumulus models. *J. Atmos. Sci.*, **30**, 879-893.

947 Soong, S.-T., and Y. Ogura (1980), Response of trade wind cumuli to large-scale
948 processes. *J. Atmos. Sci.*, **37**, 2035-2050.

949 Storer, R. L., S. C. van den Heever and G.L. Stephens (2010), Modeling aerosol impacts
950 on convection under differing storm environments. *J. Atmos. Sci.*, **67**, 3904-3915.

951 Storer, R.L., and S.C. van den Heever (2013), Microphysical processes evident in aerosol
952 forcing of tropical deep convective clouds, *J. Atmos. Sci.*, **70**, 430-446.

953 Tao, W.-K., and J. Simpson (1993), Goddard Cumulus Ensemble model. Part I: Model
954 description. *Terr. Atmos. Oceanic Sci.*, **4**, 35-72.

955 Tao, W.-K. (2003), Goddard Cumulus Ensemble (GCE) model: Application for
956 understanding precipitation processes, *AMS Meteorological Monographs - Cloud
957 Systems, Hurricanes and TRMM*. 107-138.

958 Tao, W. K. (2007), Cloud resolving modeling, *J. Met. Soc. Japan*, **85B**, 305-330.

959 Tao, W.-K., and M. Moncrieff (2009), Multi-scale cloud-system modeling. *Rev.
960 Geophys.*, **47**, RG4002, doi:10.1029/2008RG000276.

961 Tao, W.-K., X. Li, A. Khain, T. Matsui, S. Lang, and J. Simpson (2007), Role of
962 atmospheric aerosol concentration on deep convective precipitation: Cloud-resolving
963 model simulations, *J. Geophys. Res.*, **112**, D24S18, doi:10.1029/2007JD008728.

964 Tao, W.-K., J. Scala, J. Simpson (1995), The effects of melting processes on the
965 development of a tropical and a midlatitude squall line, *J. Atmos. Sci.*, **52**, 1934-1948.

966 Tao, W.-K., S. Lang, J. Simpson, C.-H. Sui, B. Ferrier, and M.-D. Chou (1996),
967 Mechanisms of cloud-radiation interaction in the tropics and midlatitudes, *J. Atmos.*
968 *Sci.*, **53**, 2624-2651.

969 Tao, W.-K. and Soong, S.-T. (1986), A study of the response of deep tropical clouds to
970 mesoscale processes: Three-dimensional numerical experiments. *J. Atmos. Sci.*, **43**,
971 2653-2676.

972 Tao, W.-K., J.-P. Chen, Z.-Q. Li, C. Wang and C.-D. Zhang (2012), The Impact of
973 Aerosol on convective cloud and precipitation. *Rev. Geophys.*, **50**, RG2001,
974 doi:10.1029/2011RG000369.

975 Tao, W.-K., S. Lang, X. Zeng, X. Li, T. Matsui, K. Mohr, D. Posselt, J. Chern, C. Peters-
976 Lidard, P. M. Norris, I.-S. Kang, I. Choi, A. Hou, K.-M. Lau, Y.-M. Yang (2014), The
977 Goddard Cumulus Ensemble model (GCE): Improvements and applications for
978 studying precipitation processes. *Atmos. Res.*, **15**, 392–424

979

980 Teller, A., and Z. Levin (2006), The effects of aerosols on precipitation and dimensions
981 of subtropical clouds: a sensitivity study using a numerical cloud model, *Atmos.*
982 *Chem. Phys.*, **6**, 67–80.

983 Thompson, A. M., W.-K. Tao, K. E. Pickering, J. R. Scala and J. Simpson (1997),
984 Tropical deep convection and Ozone formation, *Bull. Amer. Meteor. Soc.*, **78**, 1043-
985 1054.

986 Trier, S. B., W. C. Skamarock, M. A. LeMone, D. B. Parsons, and D. P. Jorgensen
987 (1996), Structure and evolution of the 22 February 1993 TOGA COARE squall line:
988 Numerical simulations, *J. Atmos. Sci.*, **53**, 2861-2886.

989 Trier, S. B., W. C. Skamarock, and M. A. LeMone (1997), Structure and evolution of the
990 22 February 1993 TOGA COARE squall line: Organization mechanisms inferred
991 from numerical simulation, *J. Atmos. Sci.*, **54**, 386-407.

992 van den Heever, S. C., G. G. Carrio, W. R. Cotton, P. J. Demott, and A. J. Prenni (2006),
993 Impact of nucleating aerosol on Florida storms. Part1: Mesoscale simulations, *J.*
994 *Atmos. Sci.*, **63**, 1752-1775.

995 van den Heever, S. C., and W. R. Cotton (2007), Urban aerosol impacts on downwind
996 convective storms, *J. Appl. Meteor. Clim.*, **46**, 828-850, doi: 10.1175/JAM2492.1.

997 van den Heever, S. C., G. L. Stephens, and N. B. Wood (2011), Aerosol indirect effects
998 on tropical convection characteristics under conditions of radiative-convective
999 equilibrium. *J. Atmos. Sci.*, **68**, 699-718.

1000 Wang, C. (2005), A model study of the response of tropical deep convection to the
1001 increase of CCN concentration. 1. Dynamics and microphysics. *J. Geophys. Res.*,
1002 **110**, D21211, doi:10.1029/2004JD005720.

1003 Wang, Y., W.-K. Tao, and J. Simpson (1996), The impact of a surface layer on a TOGA
1004 COARE cloud system development. *Mon. Wea. Rev.*, **124**, 2753-2763.

1005 Wang, Y., W.-K. Tao, J. Simpson, and S. Lang (2003), The sensitivity of tropical squall
1006 lines to surface fluxes: Three-dimensional cloud resolving model simulations. *Quart.*
1007 *J. Roy. Meteor. Soc.*, **129**, 987-1006.

1008 Yang, M.-J. and R. A. Houze, Jr. (1995), Multicell squall-line structure as a manifestation
1009 of vertically trapped gravity waves. *Mon. Wea. Rev.*, **123**, 641-661.

1010 Yin, Y., K. S. Carslaw, and G. Feingold (2005), Vertical transport and processing of
1011 aerosols in a mixed-phase convective cloud and the feedback on cloud development,
1012 *Q. J. Roy. Met. Soc.*, **131**, 221–245, doi:10.1256/qj.03.186.

1013

Table 1: Summary of precipitation sensitivity (dP) to increases in the number of CCN (dN0) for different studies. Note that van den Heever et al. [2006] used a linear CCN concentration profile that ranged from 300 cm⁻³ at 4 km above ground level to 1000 cm⁻³ near the surface; GCCN and IN effects from van den Heever et al. [2006] and Teller and Levin [2006] are excluded from the table; only five of the total 30 cases from Wang [2005] are displayed in the table. Updated and modified from Tao et al. [2007]. The results from van den Heever et al. [2011, 2013] are based on 100-day integrations using a 10,000-km domain with cyclic lateral boundary conditions, whereas Morrison and Grabowski [2011] are based on 6-day integrations, a 240-km domain, and 240 ensembles with imposed large-scale advective forcing. Note that this list of papers is not complete. This table was adapted from Tao et al. [2007, 2012].

Reference	case	dN ₀ (N _{clean}) [cm ⁻³] CNN #	dP (%)	Model specifications	
<i>Phillips et al. [2002]</i>	New Mexico	1950 (800)	-14.	1D, bin	
		4200 (800)	-30.	1D, bin	
<i>Khain and Pokrovsky [2004]</i>	Texas	40 (10)	-16.	2D, bin	
		90 (10)	-19.	2D, bin	
		290 (10)	-53.	2D, bin	
		1250 (10)	-88.	2D, bin	
<i>Khain et al. [2005]</i>	GATE	1160 (100)	-3.	2D, bin	
<i>Khain et al. [2005]</i>	PRESTORM	1160 (100)	+258.	2D, bin	
<i>Wang [2005]</i>	ITCZ	400(100)	+180.	3D, bulk	
		800 (100)	+340.	3D, bulk	
		1,200(100)	+540.	3D, bulk	
		1,500 (100)	+700.	3D, bulk	
<i>Lynn et al. [2005]</i>	Florida	1,250 (10)	-5.	3D, bin, 400x199	
<i>Teller and Levin [2006]</i>	Winter-time eastern Mediterranean	210 (100)	-27.	2D, bin	
		510 (100)	-55.	2D, bin	
		810 (100)	-73.	2D,bin	
		1,260 (100)	-93.	2D, bin	
<i>van den Heever et al. [2006]</i>	CRYSTAL	350 (300)	-22.	3D, bulk	
<i>Tao et al. [2007]</i>	TOGA COARE	2400 (100)	+58.	2D, bin, 1024 grid	
	PRESTORM	1900 (600)	-24.	2D, bin, 1024 grid	
	CRYSTAL	1900 (600)	-13.	2D, bin, >1024 grid	
<i>Fan et al. [2007a]</i>	A sea-breeze induced convective event (Houston, TX)	30,000 (3000)	+9.	2D, bin	
<i>van den Heever and Cotton [2007]</i>	METROMEX (St. Louis, June 8, 1999 convective storm)			3D, bulk	
	GCCN = 0.01 cm ⁻³	Early stage	2000 (800)	-12	3D, bulk
		Late stage	2000 (800)	-1	3D, bulk
	GCCN = 0.1 cm ⁻³	Early stage	2000 (1200)	+5	3D, bulk
		Late stage	2000 (1200)	-2	3D, bulk
	GCCN = 0.2 cm ⁻³	Early stage	2000 (1200)	+26	3D, bulk
Late stage		2000 (1200)	-1	3D, bulk	
<i>Lee et al. [2008a,b,2009]</i>	ARM-A	900 (100)	+18.	2D, bulk	
<i>Fan et al. [2009]</i>	TWP-ICE and China	1,100 (110)	+/- (Depends on the wind shear)	2D, bin	
<i>Lee and Feingold [2010]</i>	TWP-ICE	450 (50)	+9.	2D, bin	
<i>Cheng et al. [2010]</i>	A front system (Northern Taiwan)	9,000 (1000)	-12	3D, bulk	
		900 (100)	~0		
<i>Saleeby et al. [2010]</i>	Marine Warm Rain Events: January 22-23, 1998; February 2-3,	Observed AOD for each event, ranging from 0.02 to 0.7 optical depth		3D, bulk	

	2004; April 2-3, 2007 (East China Sea)			
		¼ x OBS	-38	3D, bulk
		½ x OBS	-21	3D, bulk
		Observed AOD (OBS)	-	3D, bulk
		2 x OBS	-3.5	3D, bulk
<i>Storer et al. [2010]</i>	Idealized Super Cells	100 (6,400)	-30-40	3D, bulk
<i>van den Heever et al. [2011]</i>	TOGA COARE Tropical R-C Equilibrium	25 (375) 400-1,600	+2 -6	2D, bulk
<i>Morrison and Grabowski [2011]</i>	TWP-ICE	354, 2,780, 6,130	-0.4	2D, bulk
<i>Fan et al. [2012a]</i>	AMF-China	8600 (1600)	+18% for SBM -12% for Morrison	3D, bin, 251x201
<i>Fan et al. [2012b]</i>	AMF-China: weak and strong wind shear SGP: weak and strong wind shear	1700 (280)	Weak wind shear: +7% for AMF-China (warm cloud base) and +4% for SGP (cold cloud base) Stronger wind shear: +3% for AMF-China and -4% for SGP.	3D, bin
<i>Fan et al. [2013]</i>	Long-time (monthly) simulations at TWP, SGP and Southeast China	1700 (280)	+5 to +7% at TWP and SEC -2% at SGP (decrease and increase offset). Rain rate PDF changed significantly.	3D, bin, 300x300
<i>Igel et al. [2013]</i>	North American Extra- tropical Cyclone, (Warm Front Region)	800 (400)	+1.4	3D, bulk
		1600 (400)	+2.1	3D, bulk
<i>Seigel et al. [2013]</i>	Idealized Squall Line (Africa)	~30, 125, 175 (Vertical varied with Maximum value)	~ -20-30	3D, bulk
<i>Storer and van den Heever [2013]</i>	Tropical Deep Convection (TOGA COARE)	100 (900) 800 (2400)	-25 ~+10	2D, bulk
<i>Grant and van den Heever [2014]</i>	Idealized Sea Breeze Convection (Africa)	500 (200)	-15%	3D, bulk
		2000 (200)	-40%	3D, bulk
<i>Lebo and Morrison [2014]</i>	Idealized Squall Line	100 (900)	+20 Weak wind shear	3D, bulk
<i>Kalina et al. [2014]</i>	Idealized Super Thunderstorms	100 – 10,000 100 - 5,000	-50% (low RH) + <5 % (high RH) (Depends on moist/dry condition)	3D, bulk
<i>Grant and van den Heever [2015]</i>	Idealized Supercell (moist profile)	400 (100)	~ +10	3D, bulk
		1600 (100)	~ -5	~
	Idealized Supercell (low-level dry layer)	400 (100)	~ -2	~
		1600 (100)	~ -20	~
	Idealized Supercell (mid-level dry layer)	400 (100)	0	~
		1600 (100)	~ -20	~
	Idealized Multicell (moist profile)	400 (100)	~ -1	~
		1600 (100)	~ +1	~
Idealized Multicell (low-level dry layer)	400 (100)	~ +20	~	
	1600 (100)	~ +100	~	
Idealized Multicell (mid-level dry layer)	400 (100)	0	~	
	1600 (100)	~ -15	~	

Table 2: Numerical experiments performed in this study. “P” and “T” stand for the PRESTORM and TOGA COARE cases, respectively. “low” and “high” stand for low and high CCN concentration, respectively. “Warm” is for warm rain only, and “evap” indicates reduced evaporative cooling.

Case Name	Description	Domain mean rainfall (mm)
P-low	PRESTORM continental case clean/background CCN over land	58.4
P-high	10 times CCN concentration as P-low	40.7
P-low-warm	Same as P-low except for all ice microphysics are off	60.7
P-high-warm	Same as P-high except for all ice microphysics are off	61.8
P-low-evap	Same as P-low except for evaporation is turned off from the surface to 3km, between 1 and 3 hours	51.0
T-low	TOGA-COARE maritime case clean/background CCN over ocean	19.0
T-high	10 times CCN concentration as T-low	33.0
T-low-warm	Same as T-low except for all ice microphysics are off	18.0
T-high-warm	Same as T-high except for all ice microphysics are off	24.7
T-high-evap	Same as T-high except for evaporation is turned off from the surface to 4km, between 0 and 1.5 hours	26.4

List of Figures:

Figure 1: Time series of GCE model-simulated domain mean surface rainfall rate (mm h^{-1}) for the (a) TOGA COARE and (b) PRESTORM case. The blue and red lines represent the low CCN and high CCN scenario, respectively.

Figure 2: Time-height cross sections of model-simulated domain mean total heating (K h^{-1}) for the TOGA COARE case for the (a) T-low and (b) T-high scenario. (c) and (d) are the same as (a) and (b) except for evaporative cooling (K h^{-1}).

Figure 3: Time-height cross sections of model-simulated domain mean total heating (K h^{-1}) for the PRESTORM case for (a) P-low (low CCN) and (b) P-high (high CCN) conditions. (c) and (d) are the same as (a) and (b) except for evaporative cooling (K h^{-1}). Note the color bar scales are different from the TOGA COARE case in Figure 2.

Figure 4: Profiles of domain-average microphysical heating/cooling rates: (a) total heating between 0 and 60 minutes for the TOGA COARE experiments, (b) total evaporative cooling for the TOGA COARE experiments between 0 and 60 minutes, (c) total latent heating between 60 and 150 minutes for the PRESTORM experiments, and (d) total evaporative cooling for the PRESTORM experiments between 60 and 150 minutes. The solid and dashed lines represent the low and high CCN scenarios, respectively.

Figure 5: Near surface convergence and cold pool structures for the PRESTORM case. Near surface convergence (the average from the surface to $z=3$ km) for the P-low and P-high scenarios is plotted in 5(a) and 5(b), respectively. The thin black lines in 5(a) and 5(b) indicate 0.01 mm/hr of surface rainfall and the thick black lines 5 mm/hr of surface rainfall. The middle two panels are Hovmoller diagrams of near surface equivalent potential temperature perturbation (averaged from the surface to $z=3$ km) for the P-low 5(c) and P-high 5(d) scenarios. Vertical cross of instantaneous equivalent potential temperature perturbation at 3 hours are plotted in 5(e) for P-low and 5(f) for P-high. The black contour lines indicate vertical velocities of 1 m/s, orange contours 5 m/s, and red contours 10 m/s.

Figure 6: Same as Fig. 5 except for the TOGA-COARE case. (e) and (f) are the instantaneous equivalent potential temperature perturbations at 2 hours.

Figure 7: Same as Fig. 1 except for the warm rain only simulations.

Figure 8: Same as Fig. 2 except for the warm rain only simulation.

Figure 9: Same as Fig. 3 except for the warm rain only simulation.

Figure 10: Vertical cross sections of the (a) vertical pressure gradient force (PGF), (b) buoyancy effect due to latent heat release (LHR), (c) water vapor buoyancy force and (d) water loading effect for the P-low case at 3 hours. Note that there is a difference in scales.

Figure 11: Domain mean vertical profiles of PGF [solid lines in (a)] and the LHR effect [dashed lines in (a)] for the P-low (black) and P-high (red) scenario for the PRESTORM case at 3 hours. The net effect of the PGF and LH are shown in (b) (solid lines) together with the water loading term [dashed lines in (b)].

Figure 12: Time series of surface rainfall for the PRESTORM case. The solid blue line is for the P-low case; the red solid line is for the P-high case; and the blue dotted line is the sensitivity test P-low-evap where both cloud and rain evaporation term were turned off from the surface to 3km between 1 and 3 hours.

Figure 13: Time series of surface rainfall for the TOGA COARE case. The solid blue line is for the T-low case; the solid red line is for the T-high case; and the red dotted line is the sensitivity test T-high-evap where both cloud and rain evaporation term were turned off from surface to 4km, between 0 and 1.5 hours, for the T-high case.

Figure 14: Time-height cross sections of total latent heating for the TOGA COARE case for (a) T-low, (b) T-high, and (c) T-high-evap-0.5 case where the rain evaporation rate is reduced by 50% for the first 1.5 hours from 0 to 4km.

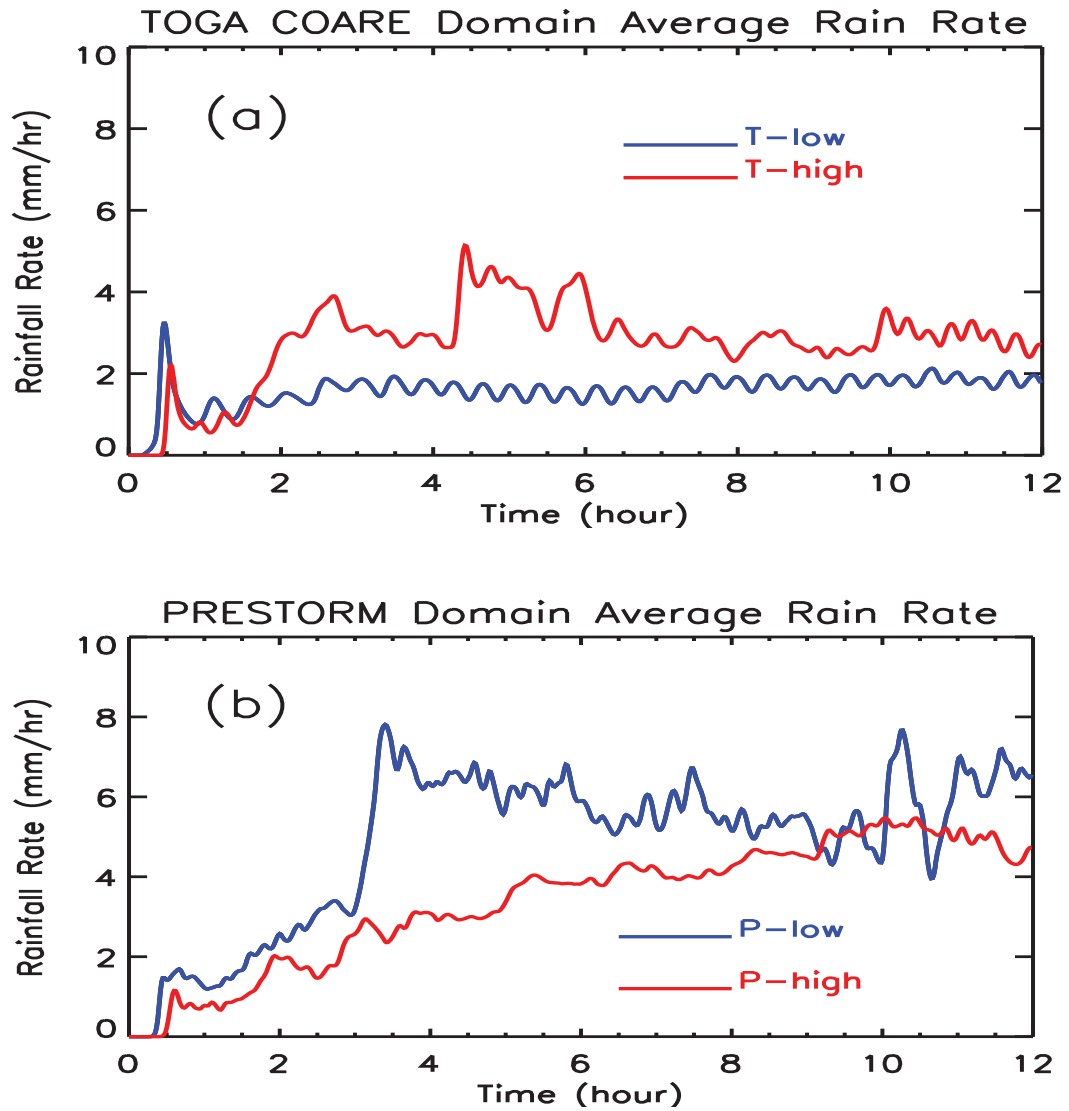


Figure 1: Time series of GCE model-simulated domain mean surface rainfall rate (mm h^{-1}) for the (a) TOGA COARE and (b) PRESTORM case. The blue and red lines represent the low CCN and high CCN scenario, respectively.

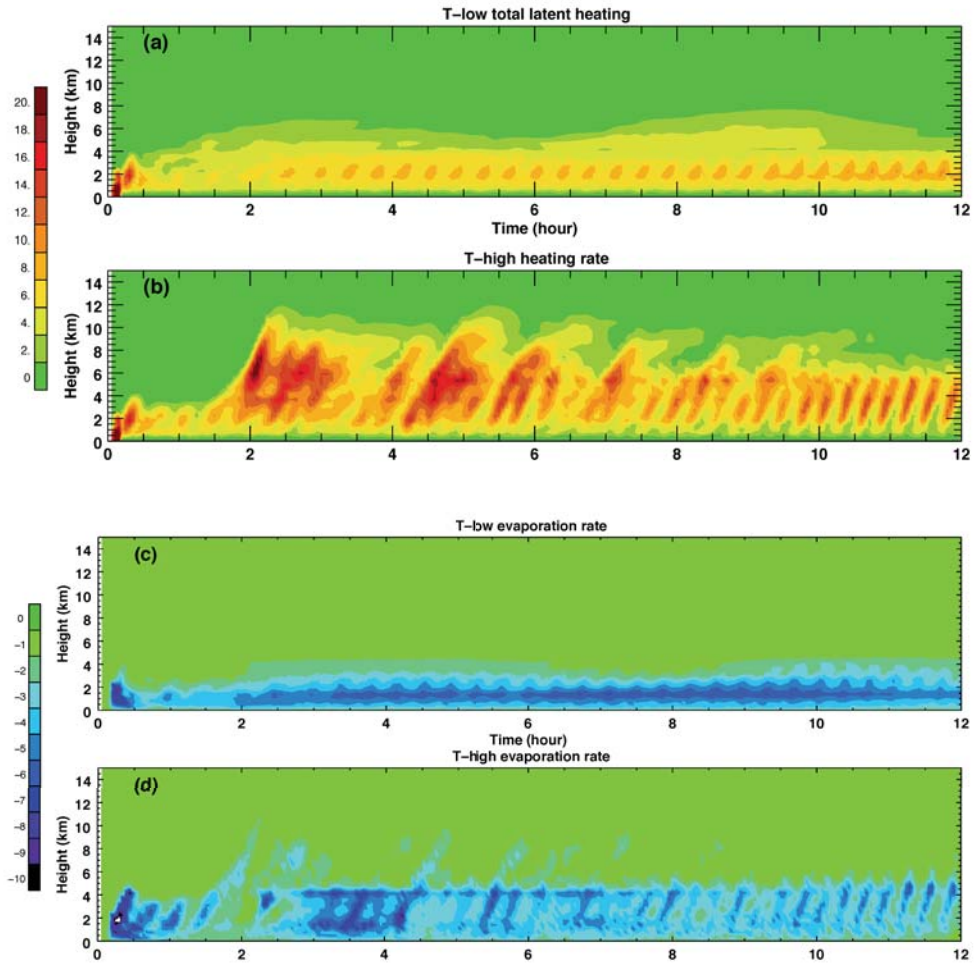


Figure 2: Time-height cross sections of model-simulated domain mean total heating (K h^{-1}) for the TOGA COARE case for the (a) T-low and (b) T-high scenario. (c) and (d) are the same as (a) and (b) except for evaporative cooling (K h^{-1}).

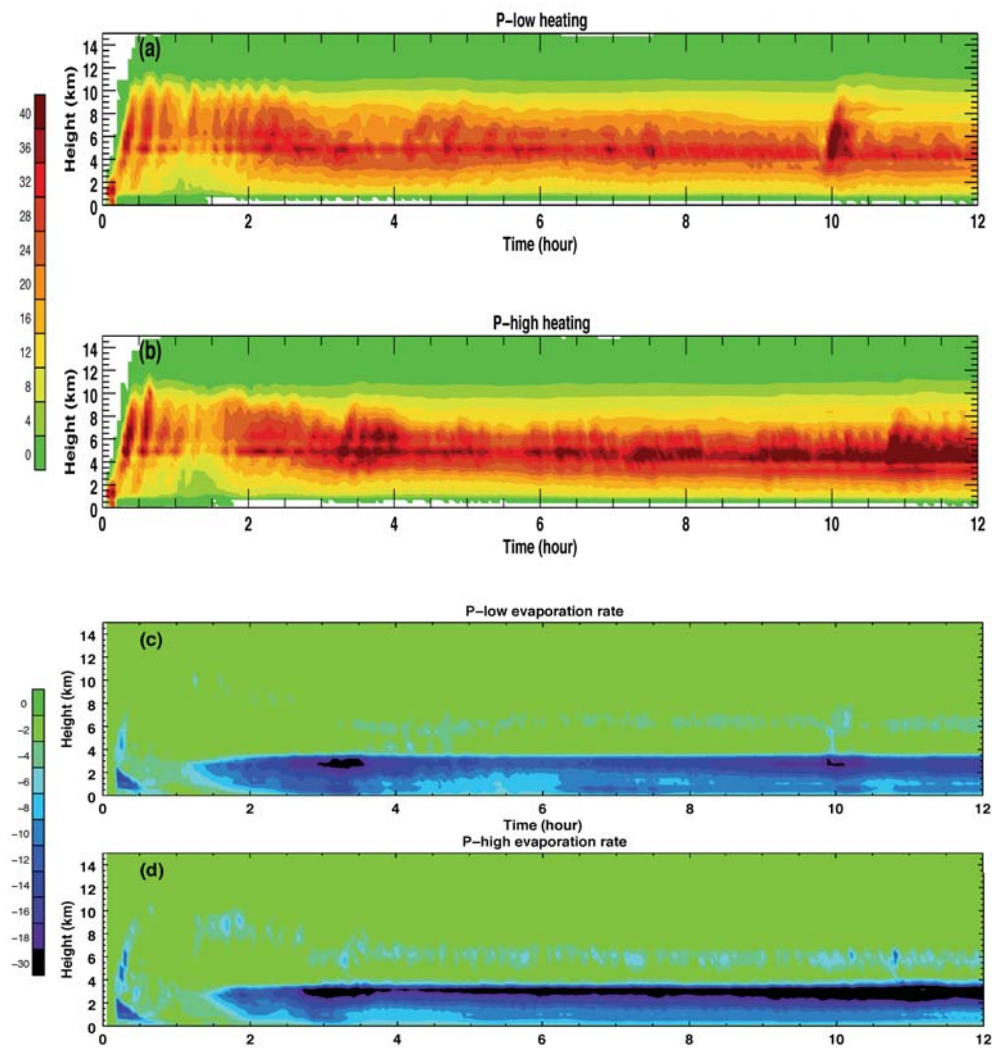


Figure 3: Time-height cross sections of model-simulated domain mean total heating (K h^{-1}) for the PRESTORM case for (a) P-low (low CCN) and (b) P-high (high CCN) conditions. (c) and (d) are the same as (a) and (b) except for evaporative cooling (K h^{-1}). Note the color bar scales are different from the TOGA COARE case in Figure 2.

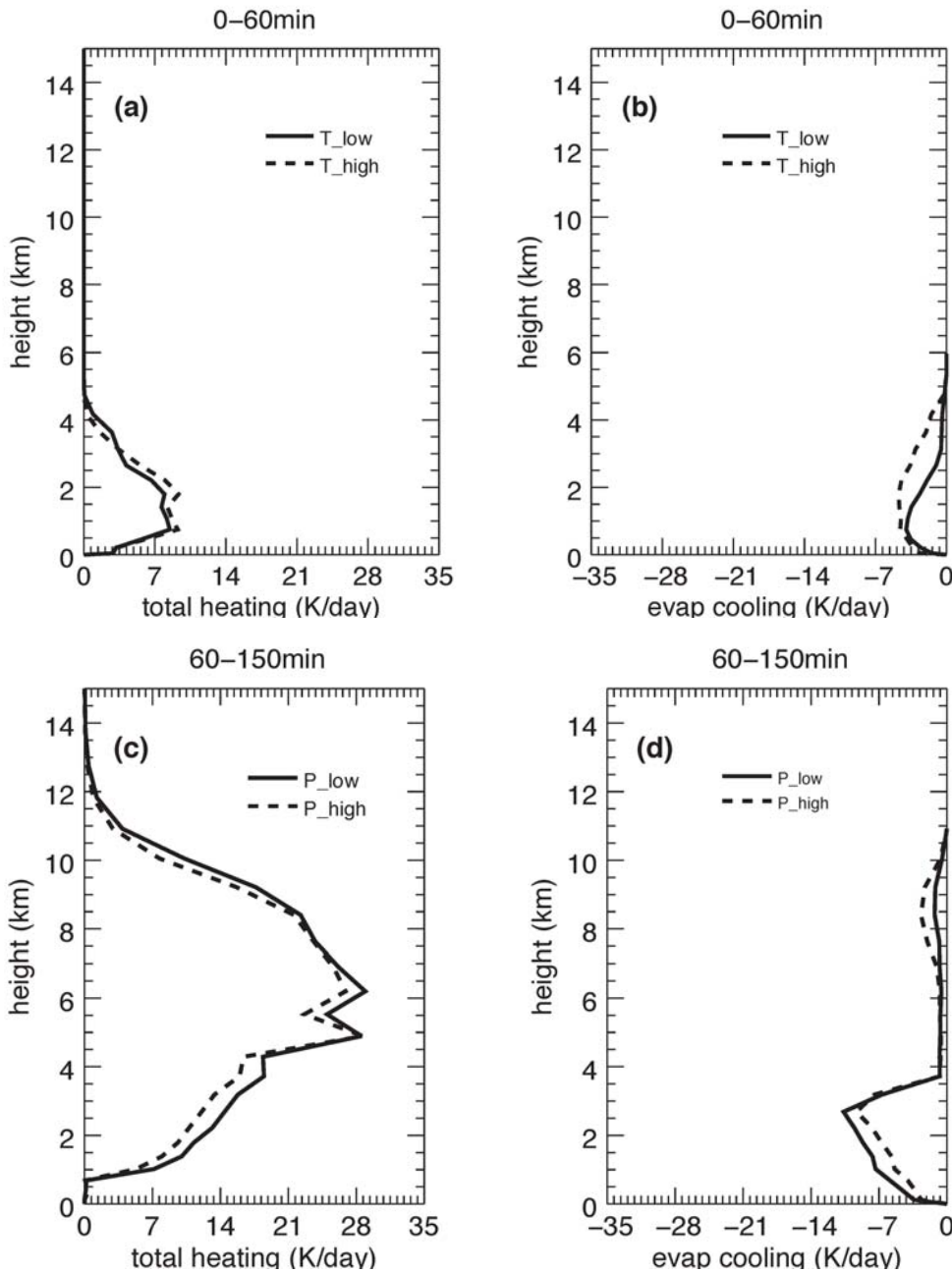


Figure 4: Profiles of domain-average microphysical heating/cooling rates: (a) total heating between 0 and 60 minutes for the TOGA COARE experiments, (b) total evaporative cooling for the TOGA COARE experiments between 0 and 60 minutes, (c) total latent heating between 60 and 150 minutes for the PRESTORM experiments, and (d) total evaporative cooling for the PRESTORM experiments between 60 and 150 minutes. The solid and dashed lines represent the low and high CCN scenarios, respectively.

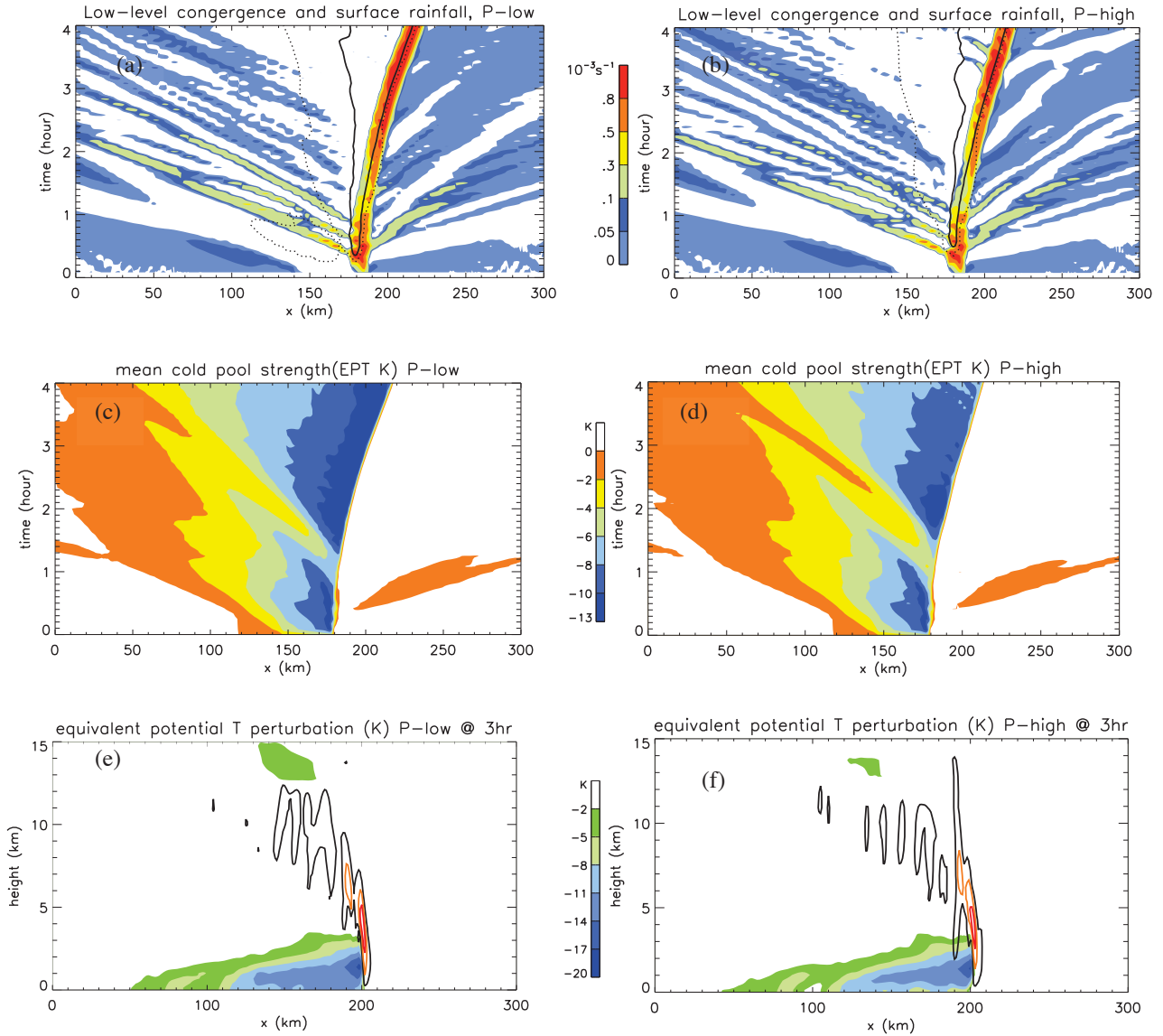


Figure 5: Near surface convergence and cold pool structures for the PRESTORM case. Near surface convergence (the average from the surface to $z=3$ km) for the P-low and P-high scenarios is plotted in 5(a) and 5(b), respectively. The thin black lines in 5(a) and 5(b) indicate 0.01 mm/hr of surface rainfall and the thick black lines 5 mm/hr of surface rainfall. The middle two panels are Hovmöller diagrams of near surface equivalent potential temperature perturbation (averaged from the surface to $z=3$ km) for the P-low 5(c) and P-high 5(d) scenarios. Vertical cross of instantaneous equivalent potential temperature perturbation at 3 hours are plotted in 5(e) for P-low and 5(f) for P-high. The black contour lines indicate vertical velocities of 1 m/s, orange contours 5 m/s, and red contours 10 m/s.

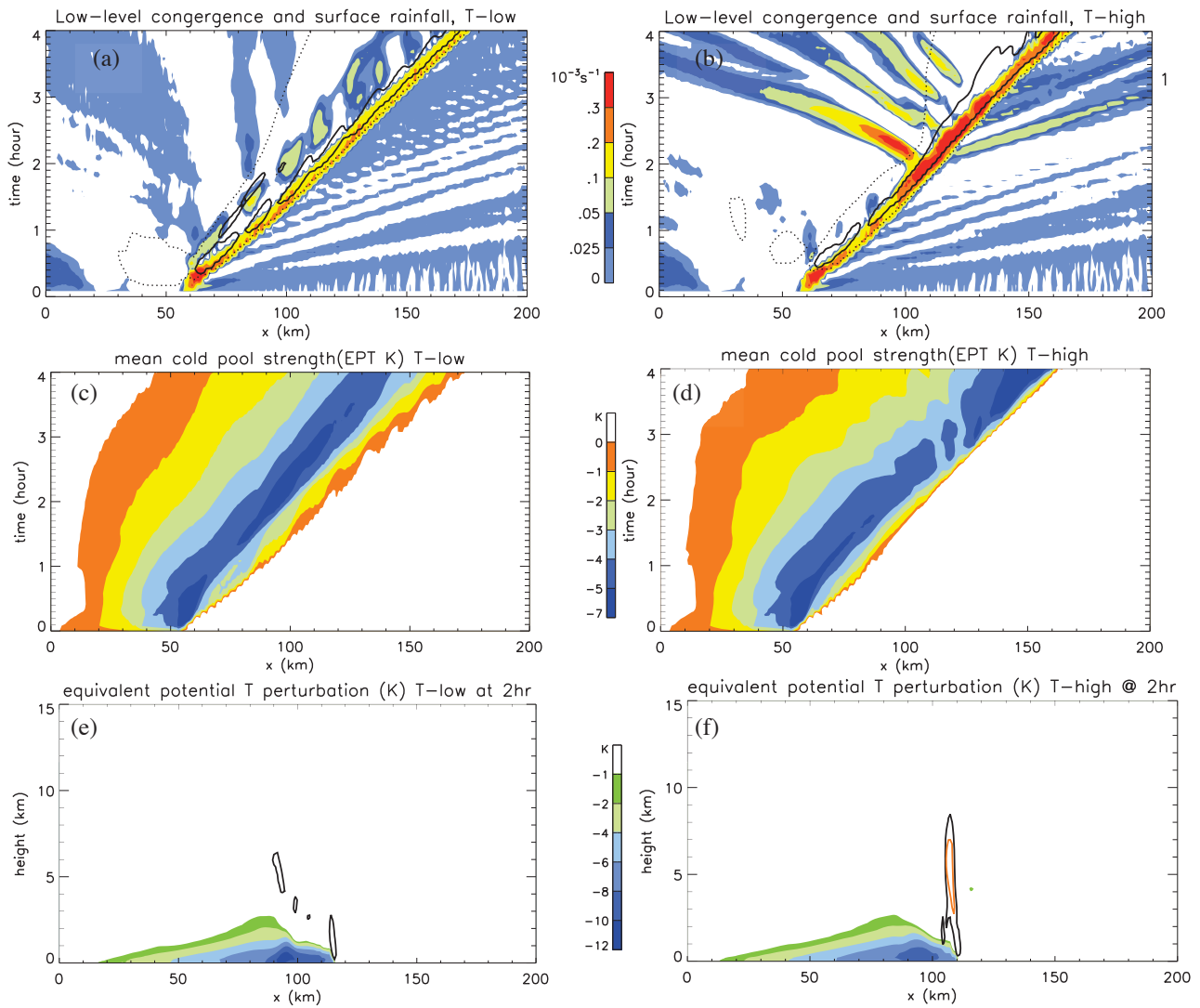


Figure 6: Same as Fig. 5 except for the TOGA-COARE case. (e) and (f) are the instantaneous equivalent potential temperature perturbations at 2 hours.

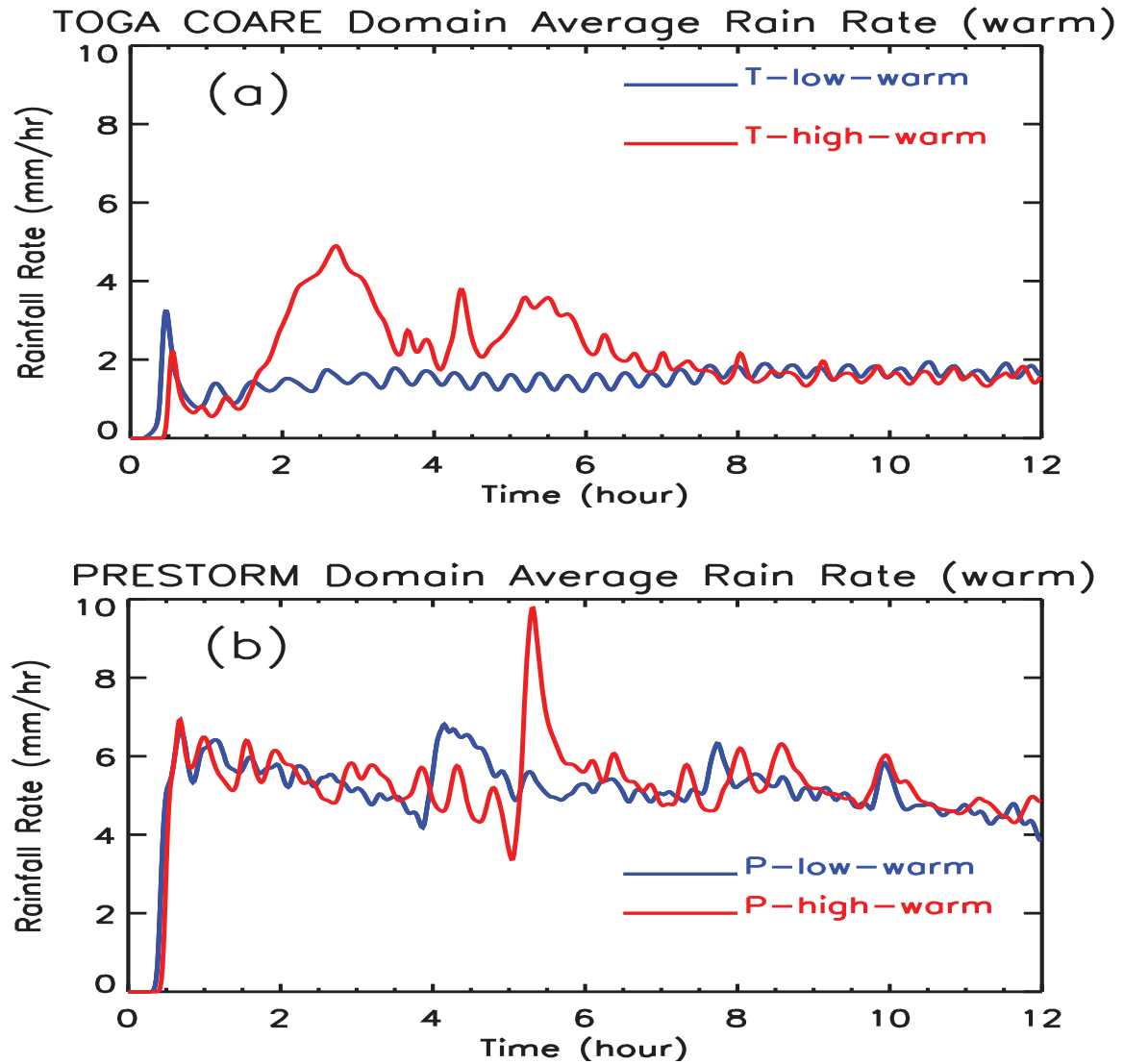


Figure 7: Same as Fig. 1 except for the warm rain only simulations.

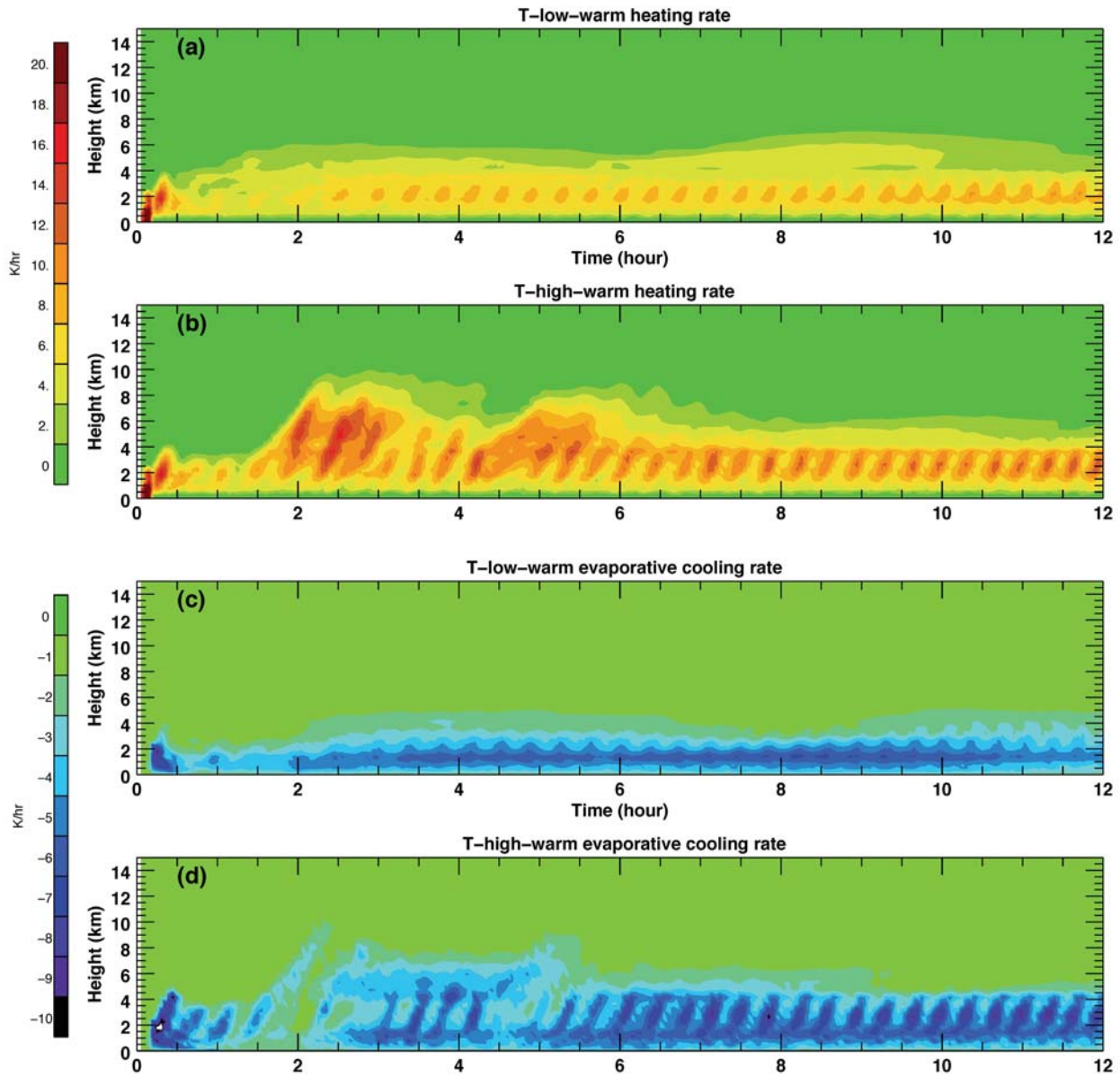


Figure 8: Same as Fig. 2 except for the warm rain only simulation.

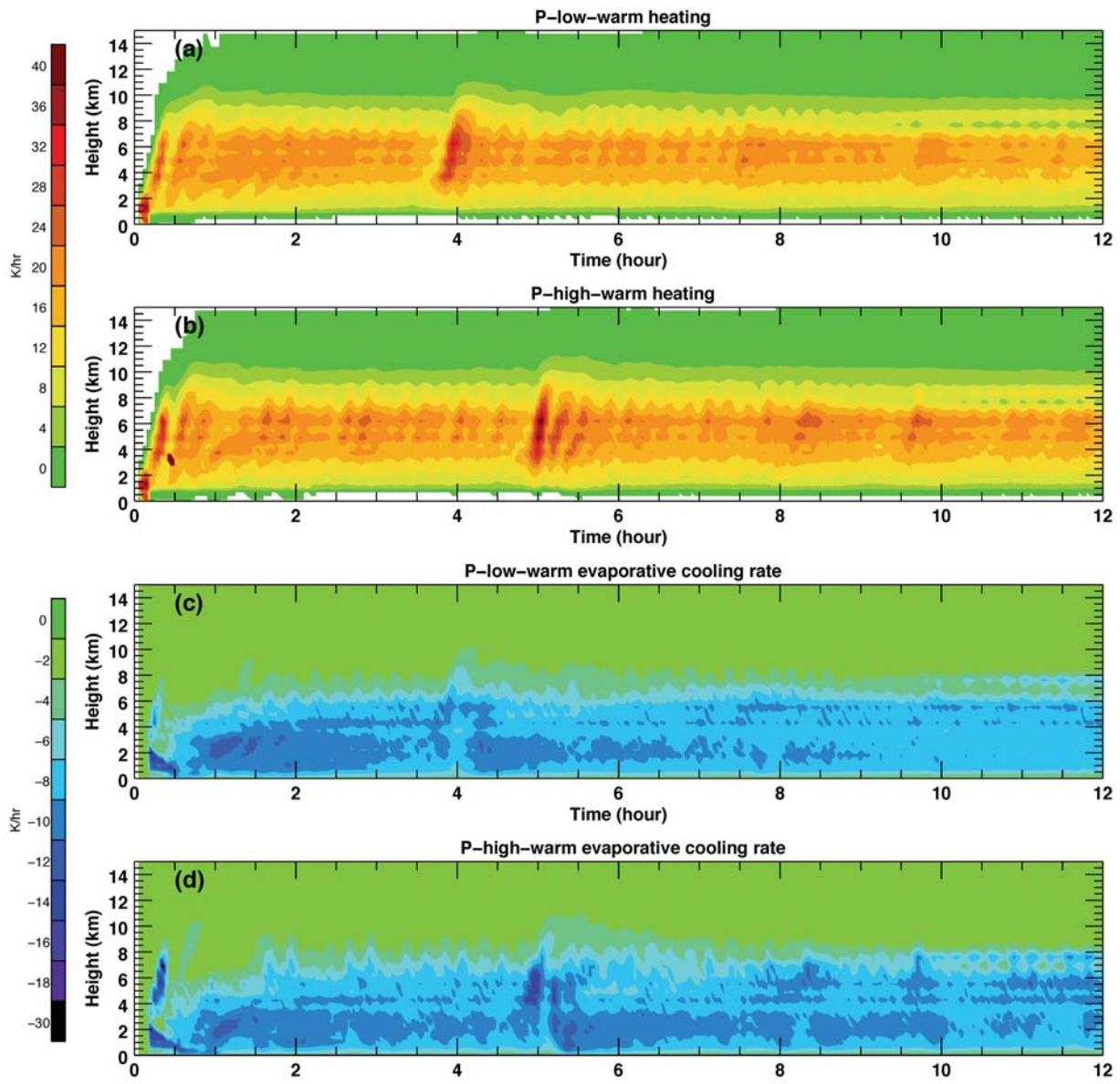


Figure 9: Same as Fig. 3 except for the warm rain only simulation.

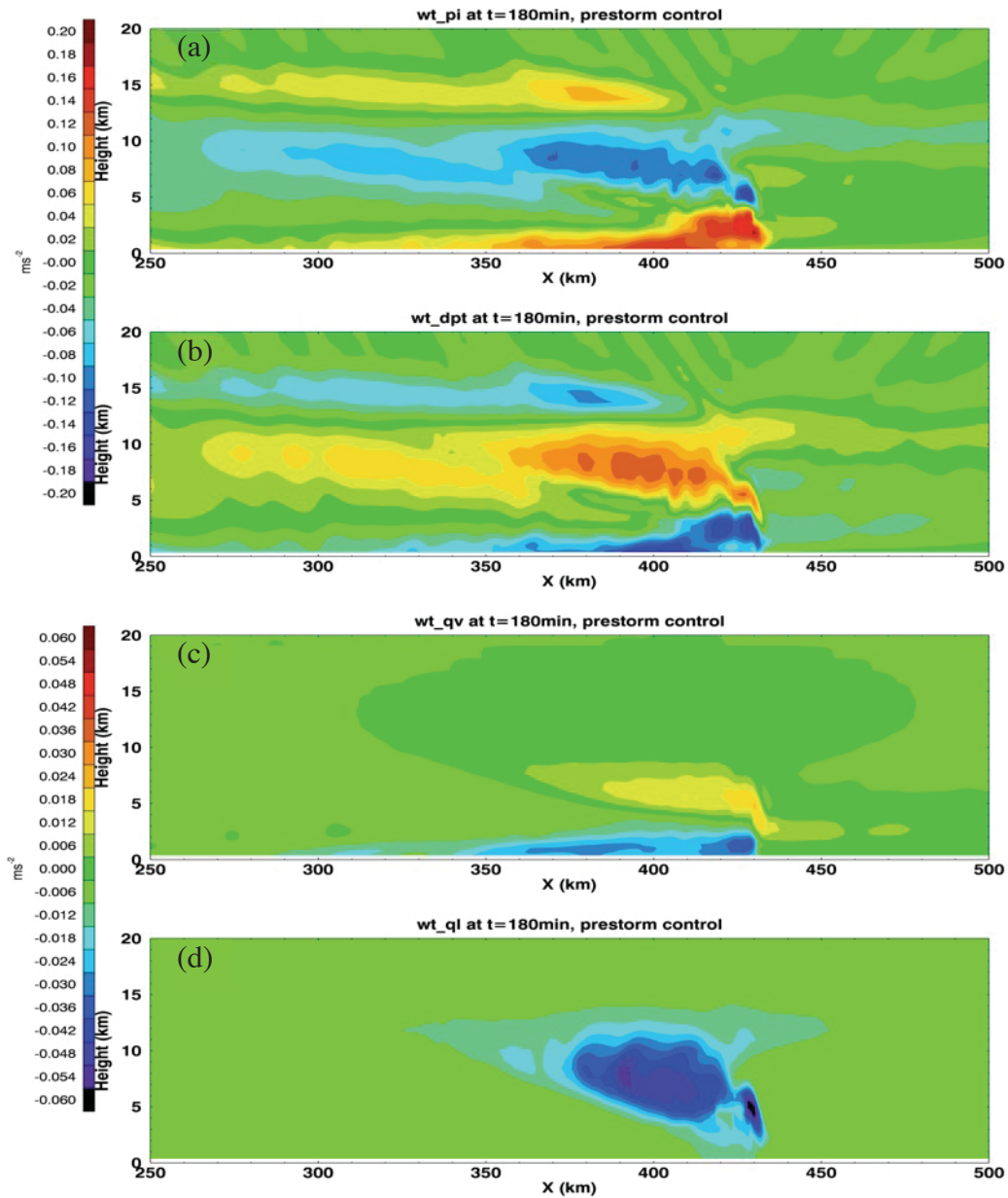


Figure 10: Vertical cross sections of the (a) vertical pressure gradient force (PGF), (b) buoyancy effect due to latent heat release (LHR), (c) water vapor buoyancy force and (d) water loading effect for the P-low case at 3 hours. Note that there is a difference in scales.

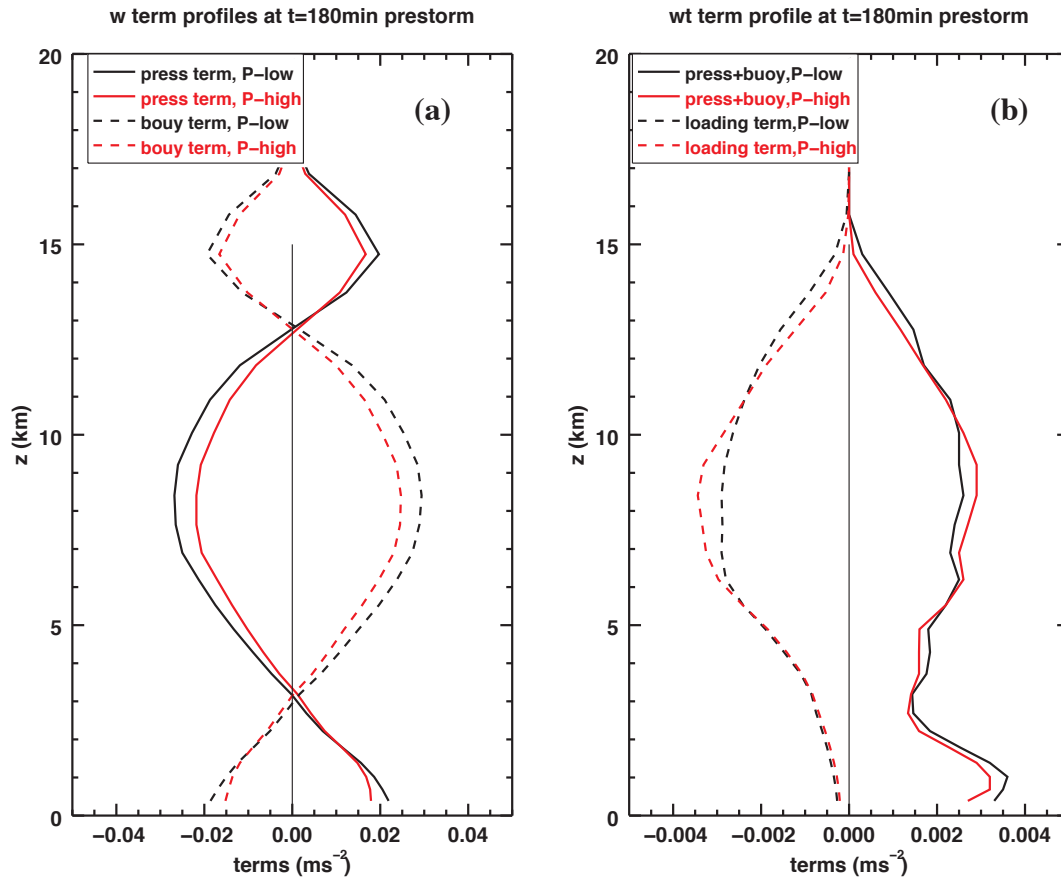


Figure 11: Domain mean vertical profiles of PGF [solid lines in (a)] and the LHR effect [dashed lines in (a)] for the P-low (black) and P-high (red) scenario for the PRESTORM case at 3 hours. The net effect of the PGF and LH are shown in (b) (solid lines) together with the water loading term [dashed lines in (b)].

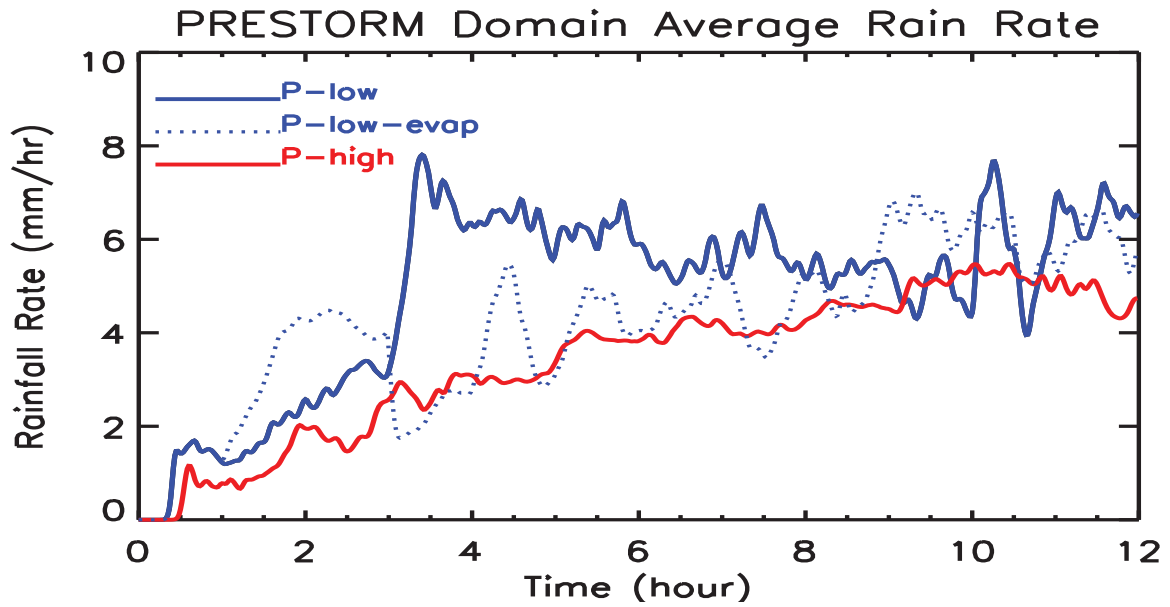


Figure 12: Time series of surface rainfall for the PRESTORM case. The solid blue line is for the P-low case; the red solid line is for the P-high case; and the blue dotted line is the sensitivity test P-low-evap where both cloud and rain evaporation term were turned off from the surface to 3km between 1 and 3 hours.

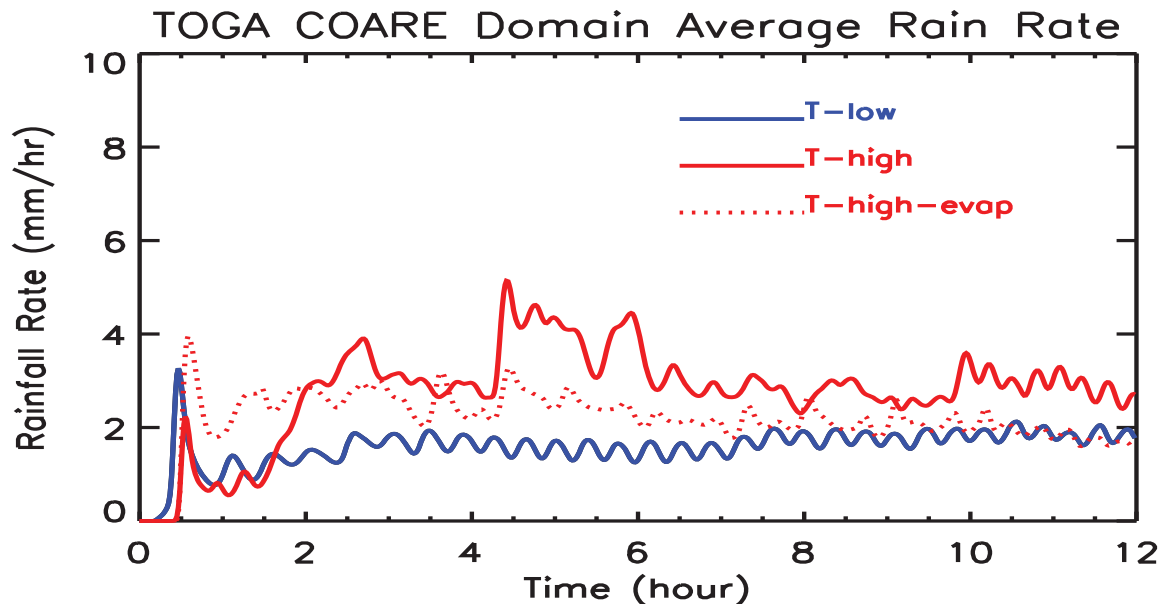


Figure 13: Time series of surface rainfall for the TOGA COARE case. The solid blue line is for the T-low case; the solid red line is for the T-high case; and the red dotted line is the sensitivity test T-high-evap where both cloud and rain evaporation term were turned off from surface to 4km, between 0 and 1.5 hours, for the T-high case.

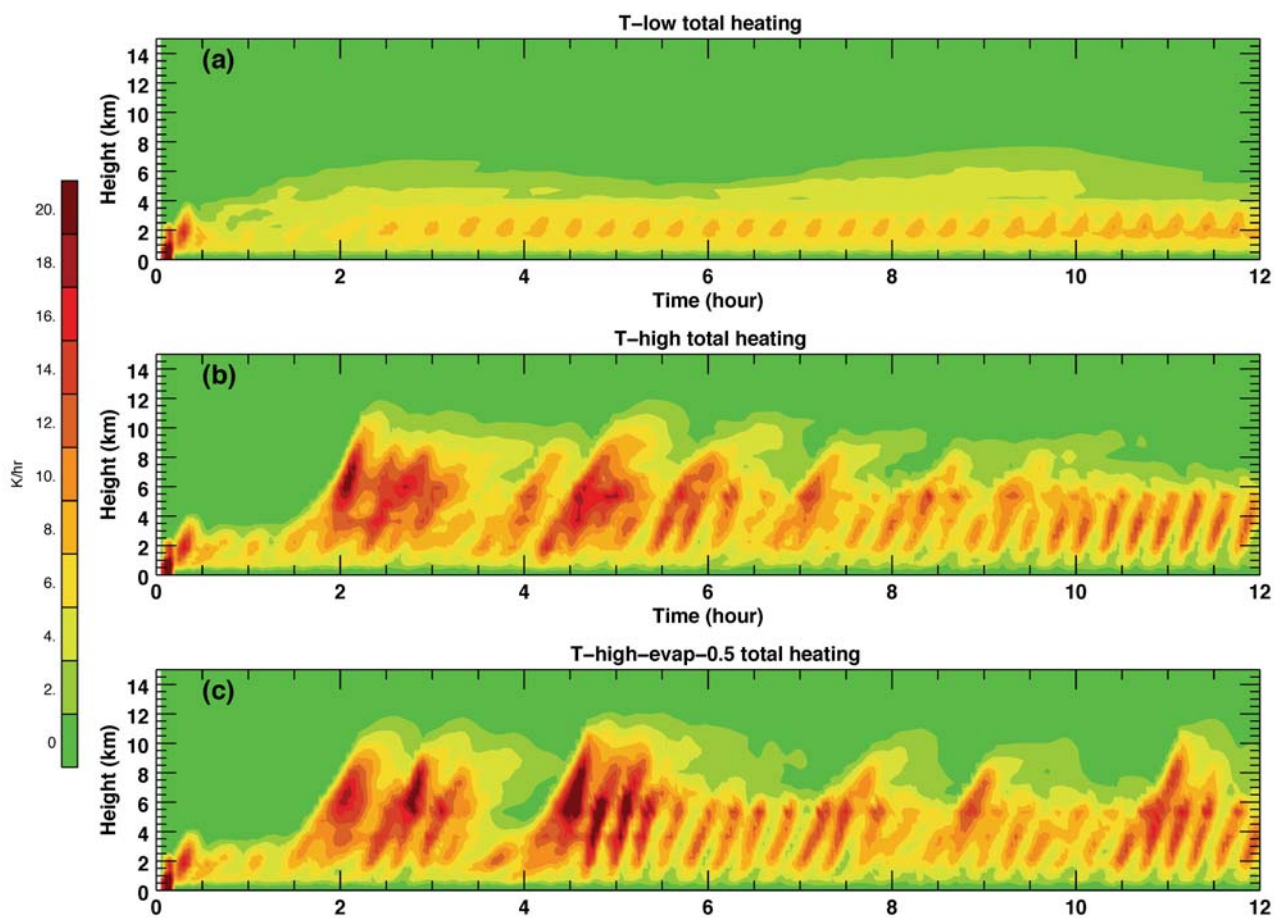


Figure 14: Time-height cross sections of total latent heating for the TOGA COARE case for (a) T-low, (b) T-high, and (c) T-high-evap-0.5 case where the rain evaporation rate is reduced by 50% for the first 1.5 hours from 0 to 4km.